

Image to Properties: Extracting Atomic Structure Information from Band Dispersion Images of Semiconductor Heterostructures Using Machine Learning

Artem K Pimachev¹ and Sanghamitra Neogi^{1,*}

¹*Ann and H.J. Smead Aerospace Engineering Sciences,
University of Colorado Boulder, Boulder, Colorado 80303, USA*

Email: sanghamitra.neogi@colorado.edu

(Dated: November 15, 2024)

The atomic environments of semiconductor heterostructures can be highly varied as various structural imperfections, lattice mismatch and non-uniform strain environments are generally present. The computational costs of first-principles modeling techniques make it challenging to fully explore how atomic environments tune the electronic bands of heterostructures. We present a machine learning (ML)-assisted first-principles modeling framework that establishes a direct relationship between the atomic environments and the electronic bands of semiconductor heterostructures. The framework combines a forward and a reverse model: The forward model predicts how the atomic environments tune electronic bands; The reverse learning model extracts information about the atomic environments that is associated with an input band structure image, such as the ones obtained with angle-resolved photoemission spectroscopy. We demonstrate the framework using silicon/germanium-based superlattices and heterostructures. Our framework offers a physics-informed approach to designing heterostructures for new phenomena and device possibilities for diverse technologies, going beyond trial-and-error approaches.

Semiconductor heterostructures, or structures composed of two or more layers of dissimilar semiconductor materials, are important condensed matter systems, both for fundamental research and for device applications [1]. The remarkable advantage of these structures is that their physical properties and functionalities can be tuned by designing the constituting layers and their interfaces. However, it is crucial to understand how the atomic structures of the heterostructures influence their physical properties to exploit the full potential of these systems. The electrical, magnetic and optical properties of materials, and the response of materials to external fields are dictated by their electronic band structures. Therefore, a complete understanding of how the electronic bands of semiconductor heterostructures are influenced by their atomic structures is essential to tune their physical properties. The atomic structures of heterostructures can be highly varied as various structural imperfections and non-uniform strain environments are generally present [2–4]. These variations of the atomic structures strongly affect the electronic bands. First-principles modeling techniques, such as density functional theory (DFT), have shown remarkable success in predicting the electronic bands of complex materials. It is necessary to use supercells as large as is feasible to include the structural complexities of heterostructures to reliably predict electronic bands. One main challenge has remained that most first-principles techniques require high computational costs to analyze large supercells. Thus, it has been prohibitive to use these techniques for analyzing heterostructures with all possible structural variations.

Furthermore, the fundamental nature of the electronic bands of heterostructures often remains uncertain. This is because the structural order of the heterostructure

could be approximately equal to those of the constituting layers or have a mixed character dictated by the imperfections. Due to the varied structural order, the supercell bands may resemble the Bloch states of either of the constituting layers or show a mixed character. Several unfolding techniques [5–10] have been proposed that could successfully identify the effective Bloch character of supercell bands of complex materials, especially alloys [11, 12]. However, only a few studies extended the discussion to heterostructures and established a predictive approach to describe the supercell bands of heterostructures. There is no first-principles approach available that can rapidly predict the electronic bands of experimental heterostructures for given atomic structures. Conversely, given the electronic bands of fabricated samples, it is highly challenging to predict which atomic structures they correspond to using existing approaches. As a result, most current research, spanning materials design, synthesis, and characterization, follows a long and expensive trial-and-error loop, making optimization challenging and precluding a link from atomic structures to electronic bands and the resulting physical properties. Fortunately, recent advances in machine learning (ML) techniques and materials science research present us with unique opportunities to disrupt these laborious processes and establish a new reverse paradigm for materials discovery and smart design.

In this article, we present an ML-assisted first-principles modeling framework that establishes a direct relationship between the atomic environments and the associated electronic bands of semiconductor heterostructures. We implement the framework using two ML models: (1) *A forward learning model* that reveals the nature of the electronic bands of a heterostructure with known

atomic structures. The forward model accepts atomic structure descriptors as input and predicts the electronic bands of the corresponding heterostructure. (2) A *reverse learning model* that identifies the structural properties of the atomic environment of the heterostructure that is associated with a given electronic band structure. The reverse model accepts computed DFT band structure images as input and predicts the corresponding atomic structure descriptors. The model can also accept images obtained with angle-resolved photoemission spectroscopy (ARPES) techniques as input and predict the corresponding structural properties. We demonstrate the forward and reverse learning framework using a class of silicon (Si)/germanium (Ge) superlattices and heterostructures. In our models, a superlattice includes one Si and one Ge layer, while a heterostructure includes multiple Si and Ge layers of varied thicknesses within one period of a model supercell. Both superlattice and heterostructure supercells have been chosen to be periodically extended. We choose silicon-based structures for their wide use in technological applications; however, our approach can be extended to other materials.

In recent years, ML-assisted approaches have remarkably accelerated materials design and discovery. However, these approaches are largely based on the forward process. One iterates over different atomic structures, uses various approaches to predict the properties, and compares the predicted properties with experimental data to design new materials. An expensive trial-and-error cycle is usually followed to design materials with desired properties for different technological applications. Our framework establishes a reverse paradigm for materials discovery and smart design by directly connecting experimental observations and first-principles modeling results. Large number of high-quality characterization images are now easily accessible due to advances in spectroscopy techniques. Our framework illustrates an approach to directly connect the experimental characterization images and atomic environments of materials. This connection provides an expedited route for designing materials with desired properties, bypassing the costly trial-and-error cycle. For example, the atomic environment descriptors predicted by our reverse learning model could be compared with structural characterization data. The comparison will provide guidance for the fabrication of structures with descriptors that result in desired electronic band structures. Our forward and reverse learning framework thus establishes a direct relationship between theory and experiment and facilitates the inverse design of semiconductor heterostructures with desired electronic band structures and, in turn, physical properties.

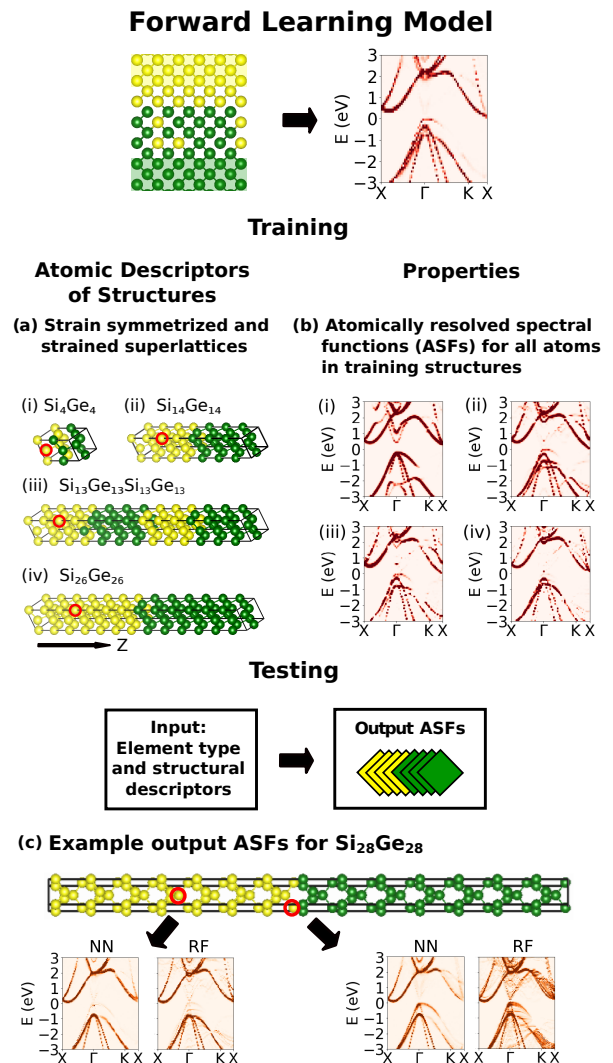


FIG. 1. **Outline of forward learning model:** (a) Training structures include strain-symmetrized and strained superlattices with various periods and compositions, such as (i) Si_4Ge_4 , (ii) $\text{Si}_{14}\text{Ge}_{14}$, (iii) $\text{Si}_{13}\text{Ge}_{13}\text{Si}_{13}\text{Ge}_{13}$ and (iv) $\text{Si}_{26}\text{Ge}_{26}$. Atomic environments of training structures are described using element type and structural descriptors. (b)(i)-(iv) Property value corresponding to descriptors: atomically resolved spectral functions (ASFs) of atoms marked with red circles in (a). Trained ML models predict ASFs of atoms in test superlattice and heterostructure, not included in training set. (c) Representative test results for $\text{Si}_{26}\text{Ge}_{26}$ superlattice. ML-predicted ASFs are validated with DFT results.

FORWARD LEARNING MODEL

Overview

Figure 1 shows the outline of our forward learning model. The training structures include Si_nGe_n superlattices with different periods and compositions, as shown in Fig. 1(a). Here, the subscript n refers to the number

of Si and Ge monolayers in a Si_nGe_n superlattice. We consider both relaxed (strain-symmetrized) and strained superlattices that represent superlattices grown on substrates [13, 14]. It is well established that lattice strain strongly influences the superlattice bands [15–17] and the resulting electronic transport properties [18–23]. We include strained structures to train the ML models on band splittings due to atomic strain. Please see Table 1 for a list of all training and test structures investigated in this work. We choose training structures such that the trained ML model could provide insight on diverse heterostructures used for technological applications. We model the training structures as ideal superlattices with sharp interfaces. We consider tetragonal supercells that are periodically extended in the [001] cross-plane direction; see Fig. 8. We optimize the geometry of supercells using DFT. We list the lattice parameters of all relaxed and strained supercells investigated in this work in Table 1 of Supplementary Materials.

The central hypothesis of this study is that direct relationships exist between the atomic environments of superlattices and heterostructures and their effective band structures. We describe the atomic environments of each atom of the supercells using the type of atomic element and a set of structural features as descriptors. We compute the effective band structures (EBS) or spectral functions (SF) of the supercells using DFT. We directly compute atomically resolved band structures (AEBS) or atomically resolved spectral functions (ASFs). Figure 1(b)(i)-(iv) show the ASFs corresponding to the atoms marked with red circles in the supercells shown in Fig. 1(a)(i)-(iv), respectively. We train the forward learning model using the two sets of data: the atomic environment descriptors of the training structures and the corresponding ASFs for each atom. The use of ASFs as training data allows us to extract large amounts of information from a limited number of training structures. ASFs not only allow us to minimize data generation efforts but also reveal fundamental insights about band dispersion in semiconductor heterostructures, as we illustrate in this article. For example, distinguishing patterns can be observed in the $E - k$ relationships of the different ASF images shown in Fig. 1(b). To test the central hypothesis, we provide descriptors of atoms of a test superlattice or heterostructure as input to the trained forward model and obtain the associated ASFs. Figure 1(c) shows example outputs of the forward model for atoms of a $\text{Si}_{28}\text{Ge}_{28}$ superlattice. We compare the ASFs predicted by ML with those computed with DFT. This superlattice structure was not included in the training set. We sum the predicted ASFs of all atoms to obtain the total SF of the test structure. Thus, we not only obtain the overall SF but also develop an understanding of how different atoms contribute to the overall SF leveraging the forward model.

The development of the forward learning model in-

cludes the following steps: (1) generation of training data of atomic environment descriptors, (2) generation of training data of ASFs, (3) implementation of ML models to identify descriptor-ASF relationships, and (4) comparison of predicted ASFs for test structures with DFT results. In the following, we describe these steps in detail.

(1) Generation of Training Data: Descriptors

The success of ML approaches for the prediction of materials properties is crucially dependent on the selection of descriptors that can establish relevant structure-property relationships [24, 25]. In our previous study, we identified a set of descriptors of semiconductor superlattice structures that have direct relationship with their electronic transport properties [22]. We trained a random forests (RF) model and analyzed the top 35 most important features of the training structures that influenced the predictions. We noticed that the elemental property features [24] minimally affect the RF predictions of the electronic transport properties. The elemental-property-based features differ only slightly across various binary (Si/Ge) heterostructures of interest. Thus, it is reasonable to expect that they do not include sufficient information to distinguish the structure-electronic property relationships. Instead, we observed that local structural features strongly affect the predicted electronic transport properties. This observation is aligned with the understanding that electronic transport in a semiconductor heterostructure is highly sensitive to local structural environments [18–21, 26]. Based on this analysis, we used only one elemental-property feature and multiple structural features in our previous study to train our RF and neural network (NN) models. Through this strategy, our aim was to instill physics understanding in the ML models and also increase their interpretability. We showed that ML models trained with these descriptors accurately predict the electronic transport properties of semiconductor heterostructures, matching experimental data [22].

In the present study, we choose one elemental and two structural features to describe each atom X in a training or test structure. We illustrate here that these descriptors have direct relationships with superlattice electronic bands. We choose the elemental feature to be the atom type: 1 for Si and 0 for Ge. To compute the structural features, we represent each superlattice and heterostructure by crystal graphs. We perform Voronoi tessellations (VT) and build crystal graphs by connecting the Voronoi cell of the atom X and the cells of neighboring atoms. We then use the crystal graphs and the tessellations to compute the following two structural descriptors [22]: effective bond lengths and order parameters.

(1) The *effective* bond length descriptor, $b_i(X)$, of atom X is given by the average of the absolute distance between the atom and each of its neighbors, n , weighted

TABLE 1. Summary of Data Used in the Forward and Reverse Machine Learning Framework

| Structure Type | Training Structures | Features | Properties | Test Structures |
|--|--|--|---|--|
| Forward Learning Model: Neural Network (NN) & Random Forests (RF) Model | | | | |
| Strain-symmetrized and strained SLs | $\text{Si}_{2p}\text{Ge}_{2p}$ $(p = 1, 2, \dots, 13)$ $(\text{Si}_{2q-1}\text{Ge}_{2q-1})^2$ $(q = 1, 2, \dots, 7)$ • 5 applied strains: [0.00%, 0.59%, 1.16%, 1.73%, 2.31%] • Total: 120 structures • Number of atoms: $6 \times 4 \times \left(\sum_{i=1}^{13} p_i + \sum_{j=1}^7 (2q_j - 1)\right) = 3360$ | • Atom type: 1 feature/atom • Effective bond lengths, b_x & b_z : 2 features/atom • Order parameters, $Q_{x,z}^{1,2,3}$: 6 features/atom • Total: $3360 \times 9 = 30,240$ features | • Spectral weights, $A^p(k, E)$: $k \times E = 64 \times 96 = 6144$ per atom (p) • Total weights: $3360 \times 6144 = 20,643,840$ | • HS: $\text{Si}_8\text{Ge}_8\text{Si}_{20}\text{Ge}_{20}$ 56 atoms Input features: $56 \times 9 = 504$ Output weights: $56 \times 6144 = 344,064$ • SL: $\text{Si}_{28}\text{Ge}_{28}$ (see SM Figure 6) 56 atoms Input features: $56 \times 9 = 504$ Output weights: $56 \times 6144 = 344,064$ (Both strain-symmetrized) |
| Reverse Learning Model: Convolutional Neural Network (CNN) Model | | | | |
| Strain-symmetrized and strained SLs | Same as Forward Learning Model | • Spectral weights, $A_{E,k}$: $k \times E = 64 \times 64$ per atom • Fermi level alignments: 13 values around -0.5 eV to +0.5 eV of mid-gap level with step of 1/13 eV • Total: $3360 \times 13 \times 64 \times 64 = 43,680 \times 64 \times 64$ <div style="display: flex; justify-content: center; gap: 20px; font-size: small;"> $\underbrace{\hspace{10em}}_{\text{images}}$ $\underbrace{\hspace{10em}}_{\text{pixels}}$ </div> | • Atom type: 1 feature/atom • Effective bond lengths, b_x & b_z : 2 features/atom • Order parameters, $Q_{x,z}^{1,2,3}$: 6 features/atom • Total: $3360 \times 9 = 30,240$ features | • HS: $\text{Si}_8\text{Ge}_8\text{Si}_{20}\text{Ge}_{20}$ strain-symmetrized Input ASFs pixels: $56 \times 64 \times 64$ Output features: 56×9 • Relaxed and strained bulk Si • Other bulk Si systems (see SM Table 2) • ARPES Si thin film For the above three cases Input ASFs pixels: 64×64 Output features: 9 |
| $(\text{Si}_{2q-1}\text{Ge}_{2q-1})^2 \equiv \text{Si}_{2q-1}\text{Ge}_{2q-1}\text{Si}_{2q-1}\text{Ge}_{2q-1}$ for odd $q = 1, 2, \dots, 7$ SL: Superlattice; HS: Heterostructure; | | | | |
| Combined Forward-Reverse Learning Framework: NN, RF & CNN | | | | |
| • Relaxed and 1.73% strained bulk Si CNN Model: Input pixels: 64×64 ; Output features: 9 NN and RF Model: Input features: 9; Output weights: 64×96 • Si ARPES spectra CNN Model: Input pixels: 64×64 ; Output features: 9 NN and RF Model: Input features: 9; Output weights: 64×96 | | | | |

by the Voronoi cell face areas, A_n :

$$b_i(X) = \frac{\sum_n \omega_{i,n} A_n * \|\vec{r}_n - \vec{r}_X\|_2}{\sum_n \omega_{i,n} A_n}. \quad (1)$$

Here, i refers to Cartesian directions, (x, y, z) , \vec{r}_X is the location of atom X , \vec{r}_n is the location and A_n is the Voronoi cell face area of the n^{th} neighbor atom, respectively. We include the factor $\omega_{i,n}$ to define direction-dependent bond lengths: $\omega_{i,n}$ selects the projections of

the face areas (A_n) along a chosen Cartesian direction (*i*). $\vec{\omega}_n$ represents the projection of Voronoi cell face area, A_n , onto the Cartesian planes:

$$\begin{aligned} \vec{\omega}_n &= (\omega_{x,n}, \omega_{y,n}, \omega_{z,n}) \\ &= (\cos^2 \phi_n \sin^2 \theta_n, \sin^2 \phi_n \sin^2 \theta_n, \cos^2 \theta_n), \end{aligned} \quad (2)$$

where ϕ_n and θ_n are the polar and azimuthal angles of the interatomic distance vectors between the atom X and the

n^{th} neighbor. We introduce the weights, $\vec{\omega}_n$, to describe the anisotropy of the bonding environments along the in-plane and the cross-plane directions of the superlattice. Note that b_i is the average neighbor distances weighed by the Voronoi cell areas projected onto the i^{th} direction. Since the areas are perpendicular to the i^{th} direction, the separation of the atoms along the perpendicular direction will affect b_i . For example, larger interatomic separations along the x direction will increase b_z and vice versa.

(2) The order parameter descriptors measure the structural order of the atomic environments and quantify to what extent the atomic arrangement in a superlattice or heterostructure differs from purely ordered or purely random distributions [27]. We construct the order parameter descriptors by adopting a modified form of the Warren-Cowley order parameters [24, 27]. We consider crystal graphs that connect an atom X with neighboring atoms of up to $order = 1, 2, 3$. We do not consider higher-order graphs since including them does not significantly affect the predictions; however, it raises the computational cost proportionally with the neighborhood volume, $\sim \text{order}^3$. We calculate the order parameter, $Q_i^{order}(X)$, of atom X by summing over the probabilities of all possible non-backtracking paths that connect atom X with neighboring atoms in a given order crystal graph:

$$Q_i^{order}(X) = \sum_{paths} \prod_{steps}^{order} \frac{\omega_{i,n} A_n \delta_{nX}}{\sum_a \omega_{i,a} A_a - \sum_b \omega_{i,b} A_b}, \quad (3)$$

where $i = (x, y, z)$. The ratio in Eq. 3 is the probability of taking each step on a given path. The numerator is the face area of the Voronoi cell (A_n) being crossed, normal to the direction of the step. The denominator is the sum over all face areas that the step could possibly cross, which are part of non-backtracking paths. The two sums in the denominator are over all allowed (a) and back-tracking (b) paths, respectively. The Kronecker delta term, δ_{nX} , is included to only select those steps that connect the atom X to neighbor n that are of the same atom types. This restriction adds species awareness to the order parameters. We include the factor $\omega_{i,n}$ to implement the directional bias as discussed before. We define directional order parameters by considering the projections of the face areas (A_n , A_a or A_b) along different directions separately while calculating the probabilities. We multiply the probabilities of each step on a given path to determine the probability of the selected path. The sum of the path probabilities yields the order parameters. For further details on the descriptors, see the extensive discussion in the Supplementary Information of Ref. 22.

Here, we illustrate that the chosen descriptors are highly effective in distinguishing the atomic environment of different atoms of Si/Ge superlattices. We show example descriptors of atoms of Si₇Ge₅ superlattice in Table 2. We use a periodic supercell of the Si₇Ge₅ superlattice to

compute the atomic descriptors. This implies that the

TABLE 2. Descriptors of Atoms of Si₇Ge₅ Superlattice

| Atom | Type | b_x | b_z | Q_x^1 | Q_z^1 | Q_x^2 | Q_z^2 | Q_x^3 | Q_z^3 | |
|-----------------|------|-------|-------|---------|---------|---------|---------|---------|---------|------|
| Si | 1 | 2.620 | 2.632 | 0.55 | 0.51 | 0.49 | 0.47 | 0.39 | 0.38 | |
| Si | 1 | 2.591 | 2.633 | 0.96 | 0.92 | 0.68 | 0.65 | 0.60 | 0.59 | |
| Si | 1 | 2.594 | 2.640 | 1.00 | 1.00 | 0.94 | 0.91 | 0.74 | 0.73 | |
| Si ₇ | Si | 1 | 2.594 | 2.641 | 1.00 | 1.00 | 0.98 | 0.98 | 0.86 | 0.82 |
| Si ₇ | Si | 1 | 2.594 | 2.640 | 1.00 | 1.00 | 0.94 | 0.91 | 0.74 | 0.73 |
| Si ₇ | Si | 1 | 2.590 | 2.633 | 0.96 | 0.92 | 0.68 | 0.65 | 0.60 | 0.59 |
| Si ₇ | Si | 1 | 2.619 | 2.632 | 0.55 | 0.51 | 0.49 | 0.47 | 0.39 | 0.38 |
| Ge ₅ | Ge | 0 | 2.686 | 2.647 | 0.53 | 0.49 | 0.46 | 0.47 | 0.36 | 0.36 |
| Ge ₅ | Ge | 0 | 2.718 | 2.647 | 0.98 | 0.95 | 0.69 | 0.65 | 0.56 | 0.55 |
| Ge ₅ | Ge | 0 | 2.715 | 2.638 | 1.00 | 1.00 | 0.92 | 0.88 | 0.58 | 0.51 |
| Ge ₅ | Ge | 0 | 2.718 | 2.647 | 0.98 | 0.95 | 0.69 | 0.65 | 0.57 | 0.55 |
| Ge ₅ | Ge | 0 | 2.687 | 2.647 | 0.53 | 0.49 | 0.46 | 0.47 | 0.36 | 0.36 |

Si atoms of the first and seventh rows of the Si₇ layer are adjacent to a Si/Ge interface. Similarly, atoms in the eighth and twelfth rows of the Ge₅ layer are adjacent to a Ge/Si interface. The middle rows in each layer represent atoms in the inner regions of the layers. Consequently, the descriptors of each column of Table 2 show a symmetric pattern: the near-interface atoms on either side of the inner atoms have identical descriptors in the Si₇ and Ge₅ layers. However, they differ significantly from the inner atom descriptors in the respective layers. In the Si₇ layer, the b_x values are the highest for the interface atoms and decrease as we go from the interface to the inner regions. To compensate, the b_z values are the lowest for the interface atoms and increase from the interface to the inner regions. An opposite trend can be observed for the atoms of the Ge₅ layer: the b_x values are the lowest for the interface atoms. b_x values increase while b_z values decrease as we move from the interface to the inner regions. Similar to the bond length descriptors, the order parameters distinguish the different atoms of the superlattice in the following way. The Q 's of all order are higher for inner atoms than for the respective interface atoms. As a reference, Q 's of all orders are equal to 1 for bulk systems due to the presence of neighboring atoms that are all of the same atom types. In comparison, a smaller number of atoms of the same species are present near the interfaces, resulting in a smaller number of connecting paths that contribute to the Q 's. Similar reasons lead to the consistently lower values of higher-order Q 's. Higher-order Q 's particularly help to distinguish between different inner atoms that have the same Q_i^1 and Q_i^2 , as can be observed from Table 2. The Q_z order parameters are lower than Q_x 's reflecting the heterogeneous stacking along the z direction. We only discuss the effective bond lengths and order parameters along the x and z directions, since the superlattices have similar structural environments along the in-plane x and y directions. We find that the descriptors along the x and y directions (b_x , b_y) and (Q_x^1 , Q_y^1), are identical for all atoms. Please

see Table 2 of Supplementary Materials where we show example descriptors of all atoms of Si_5Ge_3 superlattice.

Our formulation of crystal-graph-based descriptors is conceptually analogous to contemporary graph neural network (GNN) approaches for predicting material properties [28–30], however, there are some key differences. The GNN approaches represent a molecule or a crystalline material as a graph with nodes corresponding to constituent atoms and edges corresponding to interatomic bonds. Commonly elemental properties, e.g., electronegativity, covalent radius, etc., are used as node features and interatomic distances and/or bond valences as edge features. One then builds multiple layers of graph convolution that update the node features based on their local chemical environment and extract features that are strongly related to target properties. Although these approaches can be generalizable to many material classes, they require a large amount of training data to extract relevant features for predicting various properties. We also start by representing the heterostructures as crystal graphs with nodes corresponding to the constituent Si and Ge atoms. However, instead of extracting the node features using complex graph convolution, we assign the node features based on physics knowledge prior to training the model. We use one elemental property (atom type) and eight graph-derived descriptors ($b_{x,z}$, $Q_{x,z}^{1,2,3}$) as node features. Our physics-enforced approach allows us to train ML models with significantly less data; this is essential since the availability of electron transport property data for heterostructures is minimal in the large DFT databases [31, 32]. Furthermore, these descriptors help us reveal fundamental physics insights about the nature of electronic bands in semiconductor heterostructures and how they are affected by atomic environments. We identify which descriptors of the atomic environments have direct relationships with electronic bands and use the knowledge to establish a forward and inverse relationship between atomic environments and electronic bands. We argue that our proposed descriptors will make it easier to perform follow-up computations and experiments, thereby saving time and resources for future materials discovery, such as direct-gap systems or layered materials with desired electronic transport properties. However, we agree that further work is necessary to generalize our approach to a broad class of materials.

(2) Generation of Training Data: Spectral Functions

The electronic bands of superlattices or heterostructures are directly accessible using electronic structure calculation methods, such as DFT. It is customary to use the periodic zone representation of supercell (SC) models that include different atomic environments for the calculations. However, in most cases, the interpretation of SC energy bands is challenging due to their complexity. The

SCs of our training superlattices include a wide variety of sizes, compositions, and periods, as can be seen in Fig. 1. The different SC sizes result in highly varied electronic band structures with different numbers of bands and different folding (please see Figure 1 of Supplementary Materials). It is challenging to compare the SC bands of different training structures and interpret what effects the atomic environments of different structures have on their respective electronic bands, which is the central objective of this work. Thus, even though the SC electronic bands can be readily obtained from DFT calculations, it is not advantageous to use these bands as training data for the forward learning model. The complexity and low interpretability of the SC energy bands have also been discussed in the context of random alloys [11, 12], defects [6] and different heterostructures [7, 8, 10]. The effective band structure (EBS) or spectral function (SF) approach has been shown to be highly effective in providing interpretation of SC bands for these systems [5–12]. This approach provides easily recognizable band structures that specifically highlight how atomic relaxation and the presence of structural features affect electronic bands [6, 11]. Furthermore, as we will discuss later, the SFs allow us to compare our results with ARPES spectra and relate modeling results and experimental observations. For these reasons, we obtain SFs by unfolding the SC bands in the extended zone representation of chosen reference cells (RCs) and use the data to train the forward learning model.

Identification of appropriate RCs is particularly challenging for us, since we consider superlattices and heterostructures of different periodicity and compositions. However, it is important to note that the RC representation can be defined and unfolding can be carried out purely in a mathematical sense even when the supercells include interfaces [10]. Based on this argument, we decide on a common reference RC that resembles the primitive cell of face-centered cubic (FCC) bulk silicon and use it for all our structures. However, the RC choice is not unique, and we would like to emphasize that the insights we develop in this study are independent of the choice of the RCs. We obtain RCs from SCs by a matrix transformation, via Eq. 4 – 6. The RC lattice vectors and the corresponding BZs vary for different SCs; however, all RCs include two lattice sites. The similar-size BZs provide a common reference for comparing the unfolded band structures of different superlattices and heterostructures investigated in this study. We provide a step-by-step discussion on how we construct the RCs in the “Supercells and Reference Cells” subsection and Fig. 8 of the Materials and Methods section.

We compute the electronic bands of the superlattices and the heterostructures in the periodic zone representation of the tetragonal SCs using DFT. We perform DFT calculations using the linear combinations of atomic orbitals (LCAO) pseudopotential method, as implemented

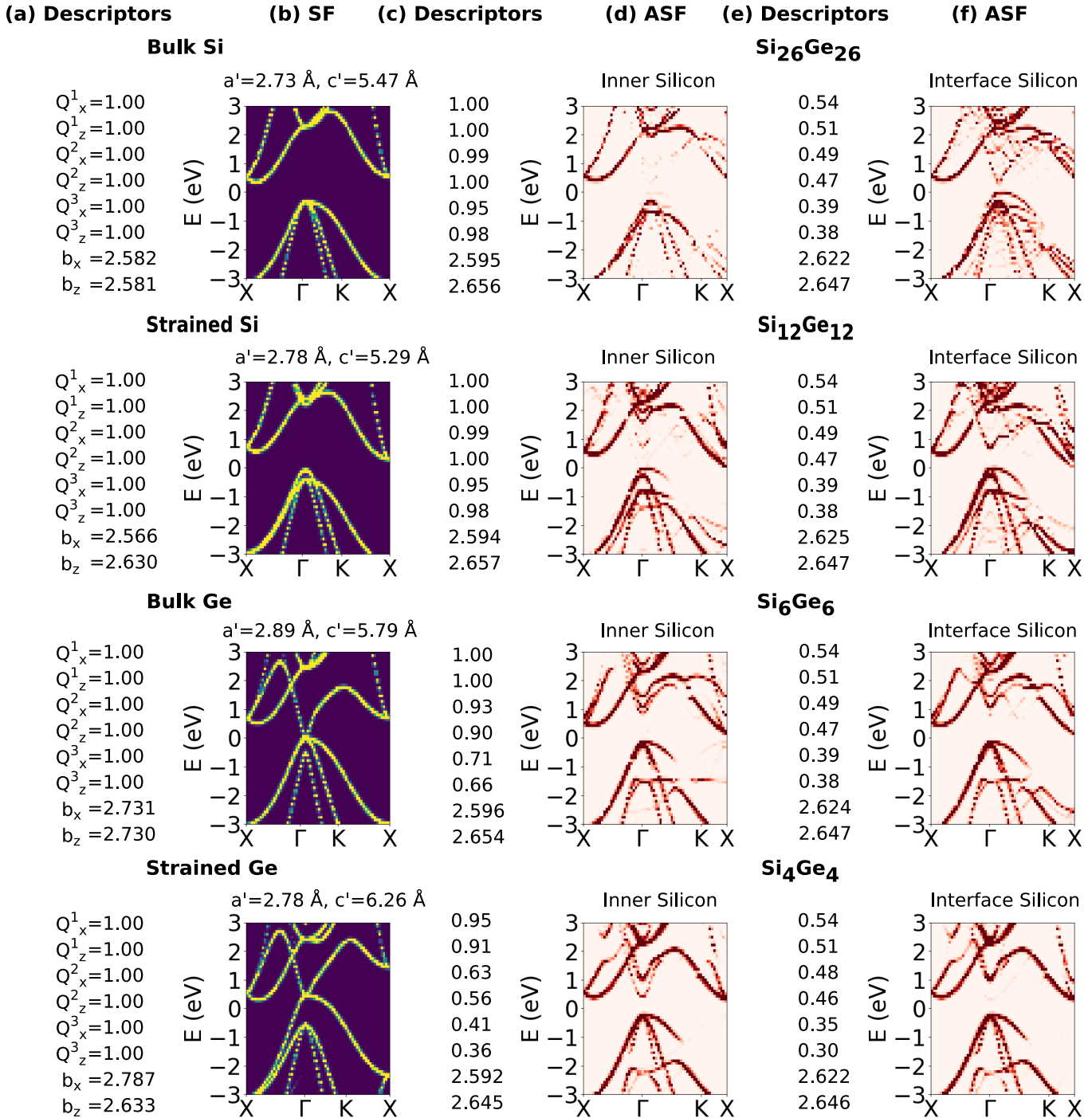


FIG. 2. Relationships between atomic descriptors and spectral functions (SFs) of Si/Ge systems investigated in this study: (a) Descriptors and (b) SFs of relaxed bulk Si (first row), strained bulk Si (second row), relaxed bulk Ge (third row) and strained bulk Ge (fourth row). Descriptors and ASFs of (c-d) inner Si and (e-f) interface Si atoms in Si₂₆Ge₂₆ (first row), Si₁₂Ge₁₂ (second row), Si₆Ge₆ (third row) and Si₄Ge₄ (fourth row) superlattices.

in the OpenMX package [33–36]. We use the Perdew-Burke-Ernzenhof (PBE) exchange-correlation formulation [37] of the generalized gradient approximation (GGA). We directly compute atomically resolved spec-

tral functions (ASFs), please see the “Spectral Weights and Spectral Functions” subsection of the Materials and Methods section for details. We compute ASFs of all atoms of the training structures along the $X - \Gamma - K - X$

path shown in the green plane in Fig. 8(f) and choose $E = -3$ to 3 eV. Figs. 1 and 10 show examples of ASFs for different training superlattices. As mentioned previously, the use of ASFs as training data allows us to extract large amounts of information from a limited number of training structures and also establish a relationship between atomic environments and band dispersion in semiconductor heterostructures, as we illustrate in the following.

Relationship Between Descriptors and ASFs

The central hypothesis of our study is that there exists a direct relationship between the structural environments of atoms of superlattices and their corresponding ASFs. We develop the forward learning model to explore this relationship, using atomic descriptors and ASF images as training data. Once trained, the forward model predicts ASFs corresponding to the input atomic descriptors of the test structures. Here, we show the atomic descriptors and the corresponding ASFs of different superlattices in Fig. 10, to develop a qualitative understanding of the relationship. We discuss how the descriptors and ASFs vary for different superlattices and also how they deviate from the respective bulk properties.

We show the descriptors and SFs of the bulk Si and bulk Ge systems in columns (a) and (b) of Fig. 10, respectively. Figure 10(a) shows that all order parameters (Q_i^{order}) of the bulk systems are equal to 1, consistent with our previous discussion. The effective bond length descriptors along the x and z directions, b_x and b_z , of the relaxed bulk Si (first row) and the bulk Ge (third row), are almost equal to each other, due to cubic symmetry. We also show results for strained bulk Si and Ge models in the second and fourth rows of Fig. 10(a-b), respectively. As we will see in Fig. 10(c-f), the descriptors-ASF relationships of the superlattices show behavior similar to that of the strained bulk systems. We model the strained bulk systems to mimic the experimental samples grown on a $\text{Si}_{0.7}\text{Ge}_{0.3}$ alloy substrate. We prepare the strained bulk Si and Ge models by fixing the in-plane lattice parameter of the supercells to those of the substrate. We list the lattice parameters of the different models on top of the SF images in column (b); see also Table 1 of Supplementary Materials for further details. The lattice parameters show that the bulk Si and bulk Ge models are tensile and compressive strained, respectively, due to substrate-induced strain. The second and fourth rows of Fig. 10(a) show that the effective bond length descriptors change for strained bulk Si and Ge models, respectively. b_x is smaller (larger) than b_z for tensile (compressive) strained Si (Ge) models. As we discussed earlier, larger interatomic separations along the x direction will increase b_z and vice versa. We observe a larger (smaller) b_z for the bulk Si (Ge) models with ten-

sile (compressive) strain in the x direction, accordingly. Note that these changes in b_x and b_z of the bulk systems are due to externally applied strains, while b_x and b_z of the superlattices are affected by internal strain due to the lattice mismatch. The internal strain is often not easy to evaluate directly, therefore, a straightforward analysis of b_x and b_z trends is not possible for superlattices. Nevertheless, the bulk results establish that the lattice strain of the atomic environments is well described by these descriptors. It is known that epitaxial strain induces splitting of the electronic bands of Si systems [38–40]. We can observe the strain-induced band splittings, especially near the Γ point, by comparing the SF images of the unstrained and strained systems shown in Fig. 10(b).

Figure 10(c-f) show the descriptors and ASFs of strain-symmetrized Si/Ge superlattices with decreasing layer thickness, $\text{Si}_{26}\text{Ge}_{26}$, $\text{Si}_{12}\text{Ge}_{12}$, Si_6Ge_6 , and Si_4Ge_4 , respectively. The columns (c)-(d) and (e)-(f) show results for atoms of the inner and interface regions of these superlattices, respectively. The contrasting information in the columns highlights how the relationships differ for different atoms within the same superlattice.

Descriptors of Inner Atoms of Superlattices: We show the descriptors of the inner atoms of the different superlattices in Fig. 10(c). The order parameters, Q 's, provide a measure of how the atomic environments differ in the inner regions of different superlattices. Q_i^1 and Q_i^2 of $\text{Si}_{26}\text{Ge}_{26}$ and $\text{Si}_{12}\text{Ge}_{12}$ superlattices are close to one, and Q_i^3 's are slightly lower than one. Both Q_i^2 and Q_i^3 of Si_6Ge_6 superlattice are smaller than one and all of Q_i^1 , Q_i^2 and Q_i^3 are smaller than one for Si_4Ge_4 superlattice. The different order Q values decrease systematically because the inner atom has a lower number of neighbor atoms that contribute to Q , in thinner layers. The Q -values indicate that the inner regions of large-period superlattices are mostly 'bulk-like' and the local atomic environments increasingly differ from bulk as we decrease the layer thickness. In the next paragraph, we discuss how the ASFs reflect a similar trend, supporting our hypothesis that atomic environments and ASFs are closely related. We also show the effective bond length descriptors of different superlattices in Fig. 10(c). They do not change significantly for the four different superlattices. However, they describe an important aspect that the inner Si regions in all four superlattices are strained because of the larger in-plane lattice parameters of the neighboring Ge layers.

ASFs of Inner Atoms of Superlattices: Figure 10(d) shows the ASFs of the inner Si atoms of the different superlattices. The first row of Fig. 10(d) shows the ASF of an inner Si atom of the $\text{Si}_{26}\text{Ge}_{26}$ superlattice. It is interesting to note that the inner Si ASF is similar to the SF image of the first row of Fig. 10(b) and shows a prominent bulk Si-like character. The electronic bands of Si/Ge superlattices are expected to have an average of bulk Si-like and bulk Ge-like characters [15, 21]. We

indeed find that the total SFs of large-period superlattices (e.g., $\text{Si}_{26}\text{Ge}_{26}$, $\text{Si}_{20}\text{Ge}_{20}$) show a mixture of bulk Si and bulk Ge-like characters (please see Figure 2 of Supplementary Materials). However, the inner Si ASFs of large-period superlattices show primarily the bulk band character. This correlates with the fact that the Q -values of inner Si atoms of $\text{Si}_{26}\text{Ge}_{26}$ are approximately equal to one, the bulk reference value. In addition to the bulk-like character, different characteristic features are present in the inner Si ASF images that distinguish them from the bulk SFs. We discuss these features in the following.

Splitting of bands: The inner Si ASF of $\text{Si}_{26}\text{Ge}_{26}$ superlattice shows splitting of bulk-like bands: The degeneracy of the valence band maxima at the Γ point is lifted and the bands are split. The valence band splitting is similar to what can be observed in the SF image of strained Si, shown in the second row of Fig. 10(b). We illustrated the strain-induced splitting of Si_4Ge_4 superlattice valence bands using first-principles studies, in our previous publications [20, 21]. The lattice strain originates in superlattices because of the lattice mismatch of Si and Ge layers, as well as growth substrates. We showed that lattice strain causes the threefold degenerate states that form the bulk Si valence band maxima to split into two approximately degenerate p_x , p_y states and one nondegenerate p_z state [15–17, 20]. The p_x , p_y states form the valence-band edge in Si_4Ge_4 and the p_z state splits off [20]. The band splittings in all four inner Si ASF images of Fig. 10(d) are induced similarly by lattice strain. However, the order of the split states and the magnitude of the splitting depend on the specific atomic environments of the different superlattices. The valence band splittings become larger for $\text{Si}_{12}\text{Ge}_{12}$ and other short-period superlattices. The splitting of conduction bands can also be seen for short-period superlattices, especially near the Γ point. Recall that the effective bond length descriptors of Fig. 10(c) show that the inner Si regions in all four superlattices are strained. Hence, the presence of the strain-induced band splittings in the ASFs supports our hypothesis about the descriptor-ASF relationship.

Mixing of bands and avoided crossing: As we decrease the thicknesses of the Si and Ge layers, the atomic descriptors increasingly deviate from bulk values. Correspondingly, the inner Si ASFs show a mixed Si-Ge character, as can be observed from the ASFs of the Si_6Ge_6 and the Si_4Ge_4 superlattices. The mixed character is contributed by two factor. (i) The different internal strain environments in the Si and Ge layers affect the bands differently. For example, the valence band edge and the split-off states differ depending on the tensile or compressive strain in the layers. (ii) The split-off bands then affect each other, for example, the split-off Si bands of $\text{Si}_{12}\text{Ge}_{12}$ and Si_6Ge_6 superlattices show a signature of avoided crossing due to the split-off Ge bands. The magnitude of the splittings is larger when the thicknesses of the Si and Ge layers are reduced, and avoided crossing

is more pronounced. Avoided crossings can also be observed in the conduction bands of Si_6Ge_6 and Si_4Ge_4 superlattices, midway along $X - \Gamma$ and $\Gamma - K - X$ paths.

Change of Γ -character: The mixing of bands increasingly influences the Γ -character of the ASFs as the superlattice period is reduced. The top valence band of $\text{Si}_{12}\text{Ge}_{12}$ superlattice displays a partial Si and a partial Ge character. The inner Si ASFs of the Si_6Ge_6 and Si_4Ge_4 superlattices also show a mixed character near the Γ point. These results demonstrate that the Γ -character of the superlattice bands strongly depends on the composition. Continuous band mixing has been demonstrated both theoretically and experimentally for alloys [41]. Here, we demonstrate the band mixing for layered heterostructured Si-Ge materials. The progression of ASF images further suggests that a direct band gap structure can be designed by tuning the composition of the heterostructures. Past studies have identified that the electronic band structure of Si_6Ge_6 superlattice has a nearly direct band gap [42] while that of Si_6Ge_4 has a direct band gap [13]. Realizing a direct band gap structure by layering two indirect band gap materials can offer various practical benefits; however, the trial-and-error process of identifying such structures can be expensive [13, 42]. Figure 10 illustrates how our framework can be used to design such a structure. Identification of the direct or indirect nature of the band gap of the Si-Ge heterostructures is out of scope for the present study because we analyze the band dispersion along a specific symmetry path.

Zone folding: Signature of zone folded bands is visible particularly for short-period superlattices when there is strong translational symmetry breaking. For example, the inner Si ASF of the Si_6Ge_6 superlattice shows a signature of folded bands along with band discontinuities. Comparing the band dispersions along $X - \Gamma$ and $\Gamma - K - X$, we can observe that ASFs show more changes along the later symmetry direction. The $\Gamma - K - X$ path spans two BZs as can be seen from the RC Brillouin zone presented in Fig. 8 in the Materials and Methods section. Therefore, varied contributions are expected to result in different features. Note that RCs are mathematical constructions and may not represent true irreducible cells for a given superlattice or heterostructure. When the chosen RCs do not capture the full translational symmetry of the supercells, residual folded bands are likely to appear.

Descriptor-ASF relationships for Interface Atoms: We show the descriptors and ASFs of the interface atoms of the different superlattices in Figs. 10(e) and (f), respectively. The order parameters of the interface atoms are all much lower than one, confirming that interface environments strongly differ from bulk. It is interesting to note that the Q -values are approximately the same for all the different superlattices discussed here. This implies that the interface atoms are in similar environments irrespective of the composition

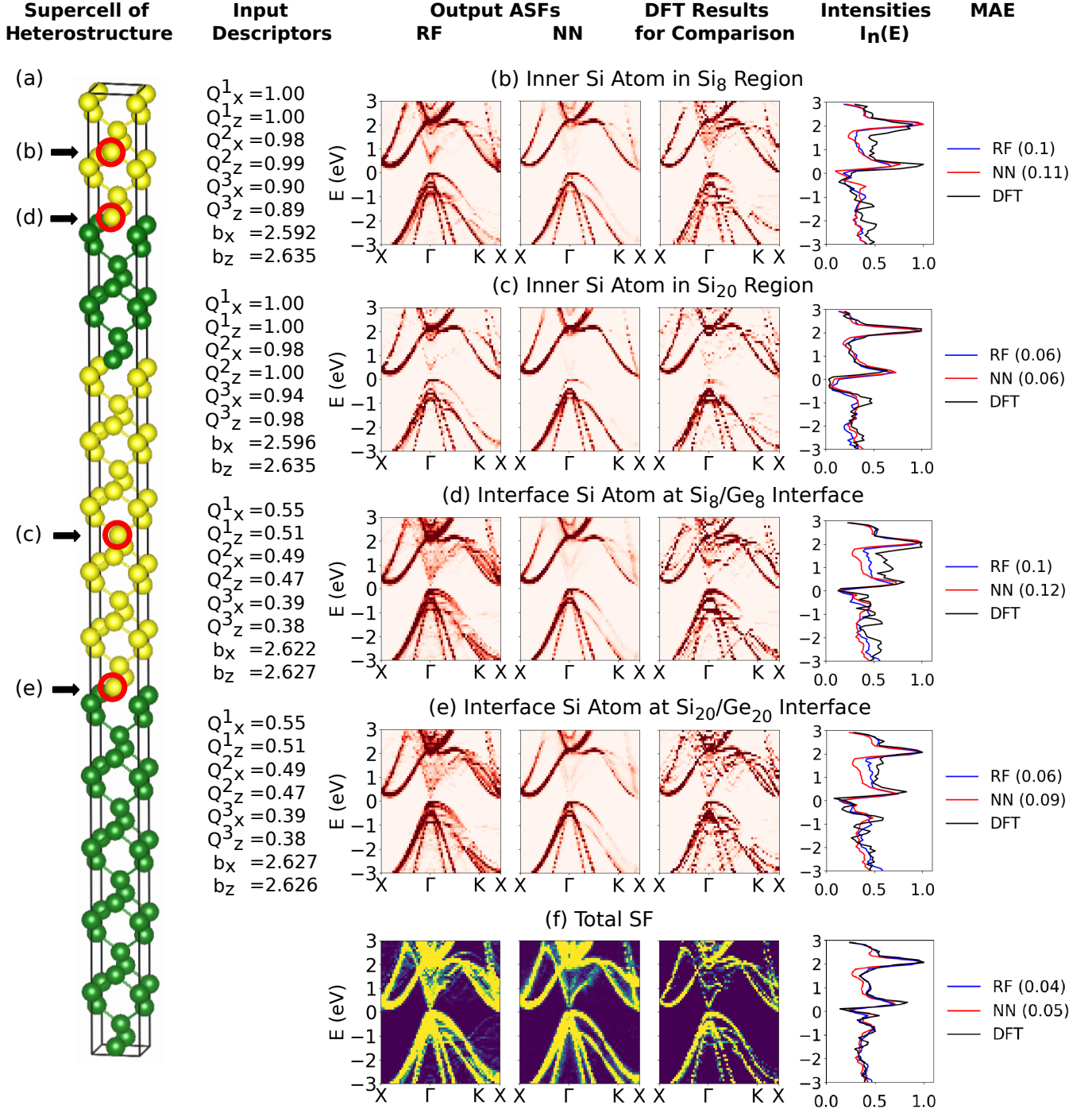


FIG. 3. **Forward learning model predictions:** (Column 1) (a) Representative supercell configuration of a test heterostructure with uneven layers: Si₈Ge₈Si₂₀Ge₂₀ and selected atoms from the (b) inner Si₈, (d) Si₈Ge₈ interface, (c) inner Si₂₀, and (e) Si₂₀Ge₂₀ interface regions of the heterostructure. (Column 2) Atomic descriptors of chosen atoms provided as input to the forward model; (Column 3 & 4) Output ASFs of chosen atoms predicted by the RF and NN models, respectively. (Column 5) ASFs of representative atoms computed directly with DFT for comparison and validation. (Column 6) Comparison between normalized intensities, $I_n(E)$, and (Column 7) MAEs for RF (blue) and NN (red) predictions. MAEs are computed between predicted and computed $I_n(E)$'s. (f) Total SF obtained by adding ASFs of all atoms of the heterostructure.

of the superlattices. Accordingly, no clear trends can be observed from the ASFs of the interface atoms. One other aspect to note is that the interface Si ASFs resemble the inner Si ASFs for short-period superlattices (Si_6Ge_6 and Si_4Ge_4). It can be argued that the inner and interface regions cannot be clearly distinguished when the Si region is only 4 to 6 monolayers in thickness.

Here, we illustrate the direct relationship between the atomic environments and the corresponding ASFs by providing a comparative discussion of bulk Si SFs and Si ASFs of different superlattices. A similar analysis can be done using the Ge ASFs of different superlattices as well (see Figure 2 of Supplementary Materials). Our analysis establishes that strain-induced band splitting, band mixing, avoided crossings, and changes of Γ -character provide a measure to differentiate the superlattice and bulk electronic bands. Quantifying these distinguishing features is critical both from the fundamental viewpoint of understanding the electronic behavior of heterostructures and for designing materials for target applications. Our forward learning model provides a direct approach to achieve both of these objectives.

(3) Implementation of ML Models

We implement the forward learning approach using random forests (RF) and neural network (NN) models, separately. The ML models are trained using the atomic descriptors and the ASFs of all atoms of the training structures. We provide a detailed description of the models in the Materials and Methods section.

(4) Comparison of Forward Model Predictions & DFT Results

We test the performance of the forward learning model using a heterostructure and a superlattice (see Figure 6 of Supplementary Materials) that is not included in the training set. We show the supercell of the test structure, $\text{Si}_8\text{Ge}_8\text{Si}_{20}\text{Ge}_{20}$, in Fig. 14(a), which includes multiple Si and Ge layers of randomly chosen thicknesses. This configuration is likely to represent fabricated heterostructures with unevenly thick layers. We perform geometry optimization of the supercell using DFT to obtain a strain-symmetrized configuration; please see the Materials and Methods section for details. We compute the atomic environment descriptors of all atoms and task the forward learning model to predict ASFs for input atomic descriptors. We choose four Si atoms from different regions of the supercell to illustrate the performance of the forward model. The chosen atoms are marked with red circles in Fig. 14(a). Figures 14(b)-(e) panels show the atomic descriptors and the corresponding ASFs of the chosen atoms, respectively. The first

column of each panel lists the order parameters and effective bond length descriptors. The atom type feature is 1 (for Si) for all examples shown, and hence we do not include it in the list. The second and third columns show the ASFs predicted by the RF and NN forward learning models, respectively. The ASFs are predicted along the $X - \Gamma - K - X$ path of the RC Brillouin zone, with k and E sampling similar to the training data. We compare the ML predictions with the respective DFT results, shown in the fourth column. Instead of comparing the ASF images, we compare the intensity, $I(E)$ at each E , obtained by adding the ASFs at different k values. We obtain the normalized intensities by dividing $I(E)$ by the maximum intensity: $I_n(E) = I(E)/\text{Max}[I(E)]$. We compute the mean absolute errors (MAEs) from: $\text{MAE}(I_n, \hat{I}_n) = \sum_E |I_n(E) - \hat{I}_n(E)|/64$. We show the comparison between predicted and computed $I_n(E)$'s in the fifth column of each panel and report the MAEs. We sum over the predicted ASFs of all atoms of the heterostructure and obtain the total SF. We show the comparison between the total SF results predicted by ML and those computed by DFT in Fig. 14(f).

Figure 14(b) and (c) panels show the descriptors and ASFs of representative inner Si atoms of Si_8 and Si_{20} regions of the heterostructure, respectively. The descriptors b_x and b_z indicate that the atoms are in strained environments. We analyze the relative importance of all descriptors in the predictions of our RF model. We note that b_x and b_z rank at the top of the list, see the feature importance plot in Figure 3 of Supplementary Materials. However, as previously discussed, it is difficult to interpret the effective bond length values. Instead, we discuss the order parameters to obtain a qualitative understanding of the results shown in Fig. 14. Figure 14(b) shows that Q_i^1 and Q_i^2 of the inner Si atom of the Si_8 region are equal to or almost equal to one; however, Q_i^3 's are smaller than one. Comparatively, Fig. 14(c) shows that all Q_i^1 , Q_i^2 and Q_i^3 of the inner Si atom of the Si_{20} region are equal to or much closer to one. The Q -values indicate that the local atomic environments in the narrow Si_8 region is less 'bulk-like' compared to the inner region of Si_{20} , as can be expected. Correspondingly, the inner Si ASF of the Si_8 region exhibits a mixed Si-Ge character with large band splittings and Ge-like bands near the Γ point. The RF prediction clearly shows the mixed Si-Ge Γ character and matches the DFT results, resulting in a smaller MAE: 0.1. However, the NN model predicts a prominent bulk Si character and faint Ge-like bands near the Γ point, resulting in a slightly higher MAE: 0.11. The prediction accuracy of both models is higher (RF:0.06, NN:0.06) for the inner Si atom in the wider Si_{20} region. The predicted inner Si ASFs show a prominent bulk Si character, corresponding to the bulk-like Q -values shown in the first column of Fig. 14(c). Due to the strained atomic environment, as indicated by the descriptors b_x and b_z , the ASFs also show band splitting, especially for

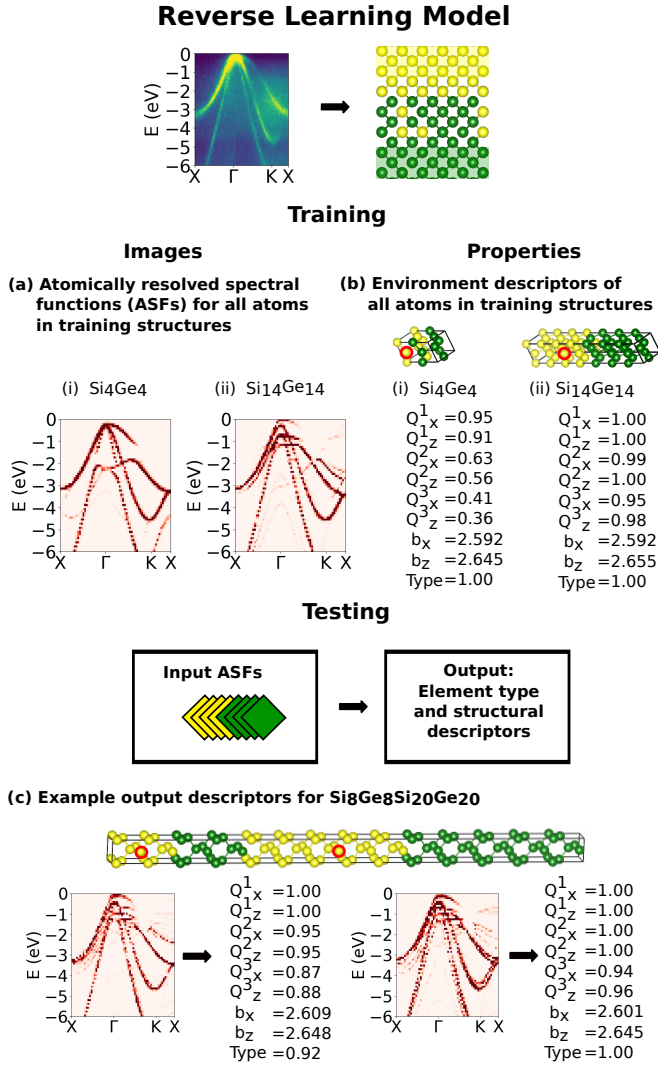


FIG. 4. **Outline of reverse learning model:** (a) Training images: Example ASFs of inner Si atoms of (i) Si₄Ge₄ and (ii) Si₁₄Ge₁₄. (b) Properties associated with training images: Element types, effective bond lengths and order parameters. Trained convolutional neural network (CNN) model predicts (c) atomic environment descriptors for input ASF of atoms in heterostructure, Si₈Ge₈Si₂₀Ge₂₀. Predictions are compared with directly DFT-computed descriptors.

the valence bands. The prediction accuracy establishes the ability of the forward learning model to predict the atomic environment-ASF relationships present in different heterostructure configurations. Note that the predicted inner Si₂₀ ASF is similar to the inner Si ASFs of large-period superlattice (Si₂₆Ge₂₆), as shown in Fig. 10. This result indicates that the inner Si atoms in Si₂₀ region are in bulk-like environments similar to the large-period superlattices. Figure 14(d) and (e) show descriptor-ASF relationships of Si atoms at the Si₈Ge₈ and Si₂₀Ge₂₀ interfaces, respectively. The Q -values of both the interface atoms are similar to each other and much lower than

one, similar to the observations we made from Fig. 10. Correspondingly, the interface Si ASFs are similar independent of the interfaces. Both show a mixed character and band splittings due to the varied strain environments near the interfaces. The RF predictions show an average character of the strain-split bands resulting in low errors (0.1, 0.06), while the NN model fails to capture the finer details and has higher errors (0.12, 0.09).

Although both RF and ML models predict accurate average characters, the DFT results (fourth column) show significantly more band splitting, mixing, and discontinuities compared to the predicted ASFs. The discrepancy can be qualitatively explained in the following way: The ML results for the different regions of the heterostructure are interpolated from ASFs of superlattices of different layer thicknesses; hence, an average character can be expected. The DFT results are not interpolated but obtained by unfolding the supercell bands in the extended zone representation of chosen RCs. It is highly likely that the RCs do not represent true irreducible cells for the given heterostructure. When the heterostructure supercell includes strongly broken translational order, the unfolded contributions from different regions may vary, resulting in broken band structures. Our training set does not include multilayer heterostructures. We expect the prediction accuracy to improve if the models are trained on such structures. Although the predicted and computed ASFs of different atoms show differences, the predicted total SFs match closely with the DFT results. The total SFs display a mixture of Si-like and Ge-like characters and have small MAEs (RF: 0.04, NN: 0.05).

REVERSE LEARNING MODEL

Overview

The forward learning model establishes that the atomic environment of each atom of a superlattice or heterostructure has direct relationship with an associated ASF. On the basis of the results of the forward model, we hypothesize that a given ASF is associated with the atomic environment in the corresponding structure. To test this hypothesis, we develop a reverse learning model that relates ASF images with the corresponding atomic environment descriptors. The model can accept both DFT-computed ASF images and experimental images obtained with ARPES techniques as input and predict the atomic environment descriptors. Thus, our work illustrates an ML-assisted approach for interpreting ARPES images and understanding how the electronic structures of nanomaterials relate to their atomic structures. Note that we train the reverse learning model with DFT data and use the trained model to extract atomic structure information from ARPES images. We acknowledge that a direct comparison between ARPES

and DFT results should be performed with caution, although both ARPES and DFT provide information on the electronic structure of materials. ARPES has the capability of directly visualizing band dispersions and Fermi surfaces by probing the energy and momentum of electrons ejected due to photoexcitation. It captures many-body effects like electron-electron interactions and electron-phonon coupling naturally, thus providing an accurate representation of the electronic structure of materials. The spectral functions obtained from DFT may not provide sufficient details of the electronic structure of strongly correlated materials and accurately represent the band gap in insulators and semiconductors. Moreover, electron lifetimes, broadening due to scattering, and band renormalization are not fully captured because DFT does not include electron-electron interaction effects. However, DFT-predicted spectral functions have been shown to match fairly well with ARPES spectra for materials with weak electron-electron correlations [43–45]. Based on these evidences, we argue that the band dispersion revealed by ARPES is equivalent to the total SFs that we discuss in this work for Si/Ge systems.

We show the outline of the reverse learning model in Fig. 4. We implement the reverse learning approach using a convolutional neural network (CNN) model; please see the Materials and Methods section for a detailed description of the model. We choose similar training structures as the forward learning model; see Table 1 for details on the training data. The training data of the CNN model includes the DFT-computed ASFs and atomic environment descriptors of all atoms in training structures. Figure 4(a) shows representative ASF images: ASFs of inner Si atoms in strain-symmetrized (i) Si_4Ge_4 and (ii) $\text{Si}_{14}\text{Ge}_{14}$ superlattices. We calculate the corresponding atomic descriptors as before, using the methods described in “Generation of Training Data: Descriptors” section. Figure 4(b) shows representative atomic descriptors of inner Si atoms of strain-symmetrized (i) Si_4Ge_4 and (ii) $\text{Si}_{14}\text{Ge}_{14}$ superlattices. We compute ASFs along the $X - \Gamma - K - X$ path of the RC BZ and for the energy range of -10 eV to 10 eV. We truncate the ASFs and use only valence bands in the energy range between -6 eV to 0 eV as training data. We treat each ASF image as a grayscale image with a resolution of 64×64 pixels, with pixel intensities scaled from 0 to 1. We choose this energy range since the literature ARPES images show this range of energy values. Additionally, we account for different Fermi level alignments by applying 13 vertical shift transformations and use the generated ASF images as training data. We include a detailed discussion about this aspect in the “Effects of Fermi-Level Alignment” section in the Supplementary Materials. We also postprocess the ASF images to create realistic training data. We apply Poisson and Gaussian noise and random level of gamma-correction (power transformation) to each image for gamma (power) in the range from 0.5 to 1.5

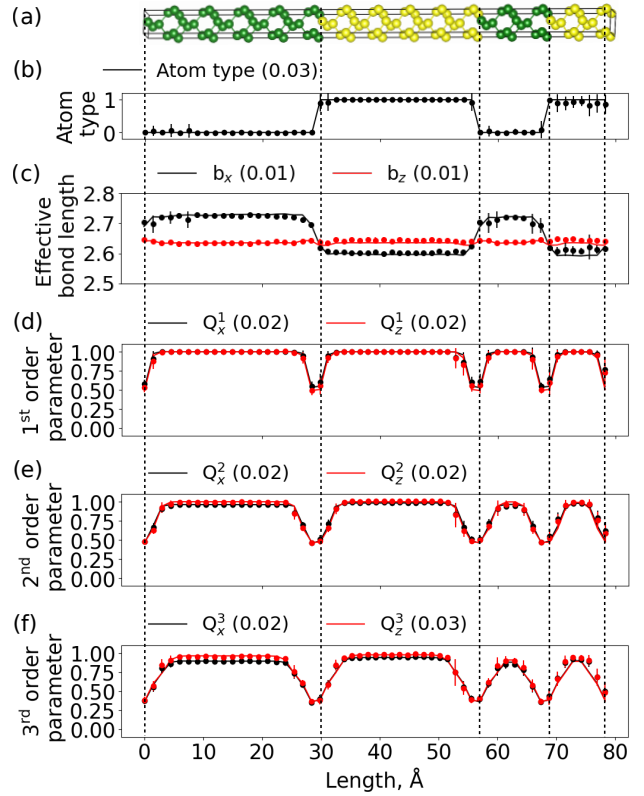


FIG. 5. **Reverse learning model predictions:** (a) Representative supercell configuration of strain-symmetrized test heterostructure, $\text{Si}_8\text{Ge}_8\text{Si}_{20}\text{Ge}_{20}$; Predicted (b) atom type, (c) effective bond length and (d-f) spatially resolved order parameters, Q_i^{order} , where $i = (x, z)$ and $\text{order} = 1, 2, 3$, for all atoms. MAEs between average predicted (circles) and calculated descriptors (solid lines) shown in panel legends. Error bars show standard deviation of predicted values for a set of input images with different Fermi level alignments.

to account for various brightness levels (signal-to-noise ratios). Training the reverse learning model with these images allows us to test the model on literature images obtained from different sources, such as different numerical computations or experiments. We test the reverse learning approach by providing ASF images as input to the trained CNN model and obtain the descriptors of the associated atomic environment. We compare the output with descriptors computed directly from structures relaxed with DFT.

Image to Properties: Example Heterostructure

We test the performance of the reverse learning model using the strain-symmetrized heterostructure, $\text{Si}_8\text{Ge}_8\text{Si}_{20}\text{Ge}_{20}$, which includes multiple layers of Si and Ge of different thicknesses. This is the same structure we used for testing the performance of the forward learn-

ing model. Figure 7 of Supplementary Materials shows the performance of the model for a strain-symmetrized configuration of the $\text{Si}_{28}\text{Ge}_{28}$ superlattice. We use the model to predict the atomic descriptors of all atoms in the heterostructure and superlattice. Figure 5 shows the (a) supercell of the test structure, $\text{Si}_8\text{Ge}_8\text{Si}_{20}\text{Ge}_{20}$, CNN-predicted (b) atom types, (c) effective bond lengths, b_x and b_z , and (d-f) order parameters, respectively. We show the CNN model predictions with filled circles and the direct DFT-derived values with solid lines, respectively. For each atom, we create a set of unique ASF images that have different Fermi level alignments and also random noise and brightness levels applied. We test the reverse learning model by providing the set of ASF images as input and obtain multiple predictions of the descriptors. Our aim is to test whether the model is able to identify physically meaningful patterns in SF images and is not sensitive to undesired image features introduced while creating the images, such as variation of brightness, random noise of experimental setup, and inherent limitation of numerical protocol followed (e.g., DFT). The error bars reflect the standard deviation of the model predictions for the set of input ASF images. Remarkably, the error bars are small for all descriptors, indicating that the model predictions are not affected by Fermi level alignment or random features in the images. We compute the MAE for each descriptor (D) using: $MAE(D, \hat{D}) = \sum_i^{p \times n} |D_i - \hat{D}_i| / (p \times n)$, where p is the number of atoms in the test structure and n is the number of Fermi level alignments applied ($n = 13$).

Figure 5(b-f) shows that the model predicts the variation of the atomic descriptors across the heterostructure with remarkable accuracy. Figure 5(b) shows that the atom types for inner atoms in thicker layers are predicted with a higher accuracy than interface atoms or atoms in thin layers. The results b_x and b_z shown in Fig. 5(c) can be understood as follows. As we discussed before, b_i is the average neighbor distances weighed by the Voronoi cell's areas projected onto the i direction. The Si and Ge layers have the same in-plane lattice constants, resulting in constant values of b_z 's (~ 2.64 Å). However, the cross-plane monolayer separations are affected by potential perturbations [20], leading to strong variations of b_x . b_x 's in Ge layers (~ 2.72 Å) are higher than those in Si layers (~ 2.60 Å), as expected. Incidentally, the effective bond length descriptors for bulk Ge and bulk Si are 2.73 Å and 2.58 Å, respectively. The slight variations can be attributed to the internal strain in the heterostructure. Figure 5(d-f) show that the order parameters of the heterostructure have a distinctive pattern consistent with our earlier discussions. All order parameter plots clearly show the interface regions: Low values of the order parameters near the interfaces indicate that the interface atoms have fewer same species neighbors. The order parameters in the inner regions of the thicker Si_{20} and Ge_{20} layers are almost equal to 1, indicating that the atomic

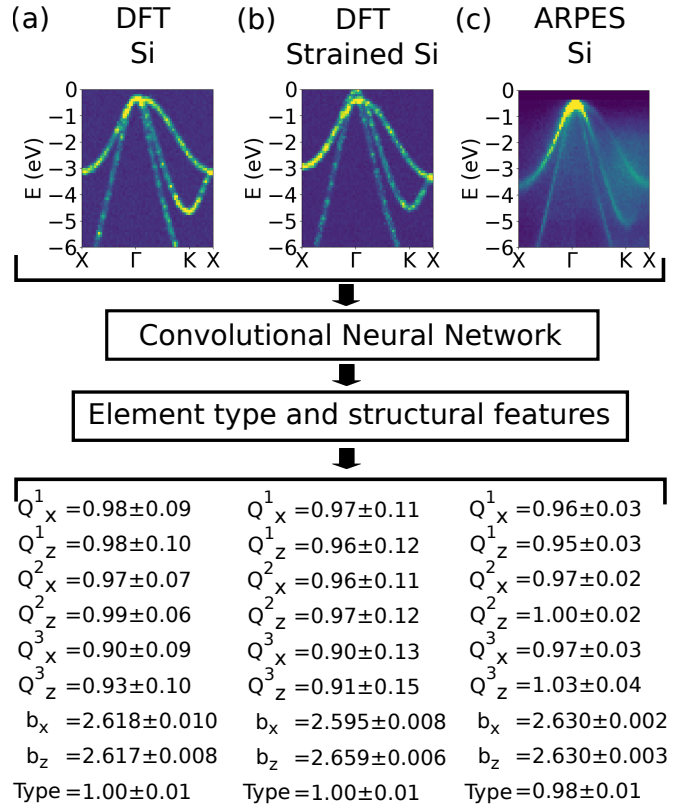


FIG. 6. **Reverse learning model predictions:** Input images: (a-b) DFT predicted SFs for (a) relaxed and (b) strained bulk Si and (c) ARPES of Si thin film, adopted from Ref. 44. CNN predicts atomic environment descriptors for input image. Standard deviations calculated for images with various Fermi level alignments and artificially applied random noise.

environments in these regions are ‘bulk-like’. Q_i^1 plots cannot distinguish the atoms in the narrow layers very well. The variation of the atomic environments in narrow layers is more clearly visible in higher order parameter plots (Q_i^2 and Q_i^3). All panels of Fig. 5 show that the model accuracy is higher for bulk-like inner regions than interfaces or thinner regions. The complex character of interface ASFs (Fig. 14(d-e)) and the limited training data result in low-accuracy predictions. Training data for the model include ASFs that are associated with varied descriptors. The CNN model learns from these fluctuations and predicts an average result that minimizes the error over all structures in the training/validation set. It is important to note that the descriptors are calculated using Voronoi tessellations that are extremely sensitive to atomic environments and introduce uncertainty in training data and predictions [46, 47]. Despite these aspects, the remarkable results confirm that the model establishes the relationship between band structure images and the atomic structures of semiconductor heterostructures.

Image to Properties: Bulk Silicon

We further test the ability of our model to extract atomic structure information from images, using multiple SF images of bulk Si. Note that the model is trained only on ASF images of superlattices and not on SF images of pristine bulk Si or Ge. We use bulk Si SF obtained from DFT as test images; the SF and ASFs are identical for a bulk Si supercell since all atoms have identical ASFs. We compute SFs of a relaxed and a strained Si supercell using DFT. The strained Si supercell is assumed to be grown on a $\text{Si}_{0.7}\text{Ge}_{0.3}$ alloy substrate, which induces 1.73% tensile strain along a' . Figure 6 shows the SF images of (a) relaxed and (b) strained Si, respectively, plotted along the $X-\Gamma-K-X$ path of the bulk Si BZ. The strain-induced splitting of the valence band maxima can be noted from Fig. 6(b). This image is similar to the one shown in the second row of Fig. 10(b). Similar to the previous test case of the heterostructure, we create a set of test images with various Fermi level alignment and random noise. Figure 6(c) shows the SF image of a Si thin film obtained using ARPES. We adopt the ARPES image from Fig. 6.2 of Ref. 44: The reference image had the ARPES spectra split into multiple panels showing different symmetry directions. We combined the different panels in one image and use that as our test image. We also apply vertical shift to the ARPES image with small increments to generate cases for different Fermi level alignments. We list the CNN-predicted descriptors for the different images in Fig. 6. The errors reflect the variation of predictions for input SF images with different Fermi level alignments, random noise, and brightness. For all three cases, the predicted order parameters are close to the bulk values of 1.00 and the atom type is predicted accurately to be Si. It is remarkable that the model associates the test SF images with atomic environments of bulk configurations without atomic interfaces. The model seemingly recognizes that the SF images do not show any signature of band mixing and makes predictions accordingly. For both (a) relaxed Si DFT and (c) ARPES image, the model predicts that $b_x = b_z$ within errors, indicating that the SF images represent high symmetry environments. b_z is higher than b_x for the strained Si system with strain along a' . We consider multiple strained bulk Si systems and test the model using the DFT-computed SF images. The model accurately predicts trends associated with all the strained systems. We include these results in Table 3 in the Supplementary Materials. We show the comparison between predicted and directly computed descriptors in Table 3 of Supplementary Materials. The predicted b_x and b_z values are somewhat higher than the DFT results, however, all trends are accurately reproduced. The results shown in Fig. 6 illustrate that the model is capable of extracting information about the atomic environment of the underlying structures from the SF images.

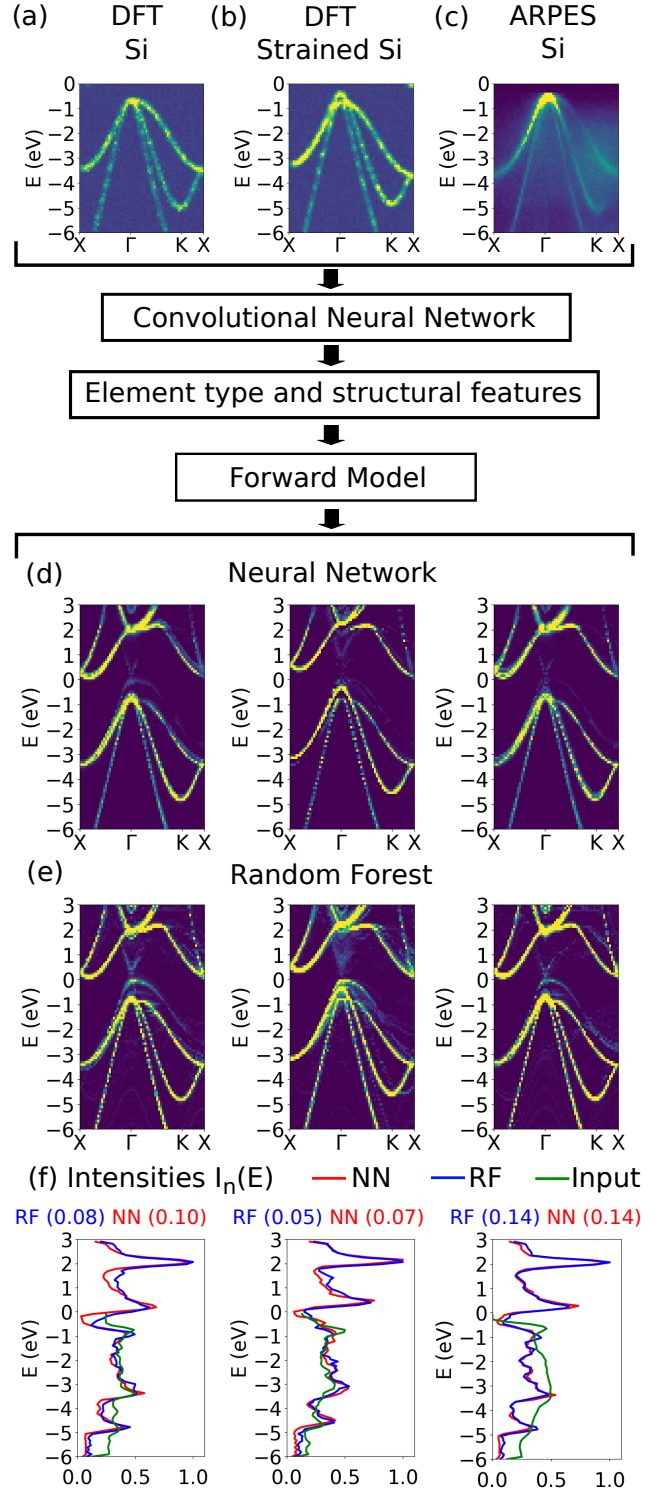


FIG. 7. **Combined forward-reverse learning framework.** Input images: (a-b) DFT SFs for (a) relaxed and (b) strained bulk Si and (c) ARPES spectra of Si thin film [44]. CNN extracts atomic descriptors from input. Descriptors are input to forward learning model. (d) NN and (e) RF output SFs of corresponding systems. (f) Comparison between normalized intensities of predicted and input SF images, respectively. MAEs are shown on top of figures.

Image to Properties: Combined Forward-Reverse Learning framework

Finally, we combine forward and reverse learning models into one framework that can (1) extract information on the atomic environment from test SF images and (2) use that information to predict SFs that can be compared with test images for additional validation of the framework. We show the workflow of the combined framework in Fig. 16 using the example of the bulk Si systems discussed in Fig. 6. The CNN model reduces the input SF images to a set of atomic environment descriptors (listed in Fig. 6). We input the CNN-predicted descriptors into the forward learning RF and NN models. Figure 16(d-e) shows the corresponding SFs predicted by the forward learning model. Note that the forward learning model can predict both the conduction and the valence bands, since it is trained with DFT images that include the bands. Forward models, particularly RF, predict faint signatures of band mixing in the Γ region, since such features are present in the training data of superlattice ASF images. We compare the outputs of the combined model with the input images to validate the combined framework. We compute the normalized intensity, $I_n(E)$, at each E and compute the MAEs between the predicted ($I_n(E)$) and input data ($\hat{I}_n(E)$) from: $MAE(I_n, \hat{I}_n) = \sum_E |I_n(E) - \hat{I}_n(E)|/64$. Fig. 16(f) shows the comparison between normalized intensities of the input and output SF images. We find close agreement for both the DFT and ARPES bulk Si test images. The higher error in the ARPES case could be attributed to the discrepancy between the quality and brightness of the training and test images. Nevertheless, this test illustrates the remarkable ability of our framework to relate electronic bands with structural information of semiconductor systems. Our framework can be particularly beneficial for interpreting ARPES images; for example, in case of delta-doping (As or P), the Fermi level shifts and the conduction bands might not be visible in ARPES images before doping but might be afterwards [44]. Our model can be used for identifying or predicting the conduction bands in ARPES experiments for different doping.

DISCUSSION

We demonstrate a ML-assisted first-principles modeling framework that enables us to establish a direct relationship between the atomic environment and electronic bands of semiconductor heterostructures. The framework combines an forward and a reverse ML model. We developed the framework to explore the relationship between the atomic environment and atomically resolved spectral functions or effective band structures of heterostructures. The forward model predicts how the atomic environments, such as neighbor bond lengths, lo-

cal network of atoms etc, tune electronic bands of heterostructure. The model predictions establish that different atomic environments contribute differently to determine the Bloch character of heterostructure bands. For example, an inner atom contributes bulk-like character; however, an interface atom introduces complex features such as band splittings, avoided crossings, and changes of Γ -characters. Based on the insights from the forward model, we develop the reverse learning model that extracts information about the atomic environment that is associated with an input band structure image. It is remarkable that the model can differentiate the structures corresponding to the SF images to be bulk configurations or ones with atomic interfaces. The combined model illustrates that atomic environments can be designed to tune heterostructure bands and achieve desired electrical, magnetic and optical properties. Our framework offers a physics-informed approach to create layered materials for new phenomena and device possibilities for diverse technologies. We anticipate that our framework will be highly beneficial to a wide research community since it can be used for achieving a variety of objectives, such as: direct comparison between modeling (e.g., DFT) results and experimental (e.g., ARPES) data, (2) evaluating limitations of modeling techniques for predicting electronic bands of complex materials, (3) interpreting ARPES spectra leveraging direct comparison between modeling and experimental results, (4) analyzing contributions from different constituting layers to heterostructure bands, and (5) inverse design of direct band gap semiconductors or broadly, new materials with desired electronic, magnetic and optical properties.

DATA AVAILABILITY

All data needed to evaluate the conclusions in the paper are present in the paper and/or the Supplementary Materials. In addition, we uploaded an example data set in the CUantamLab public GitHub repository [48]. The example data set includes geometry optimized 49 Si/Ge superlattice configurations, both strain-symmetrized and with external strain.

CODE AVAILABILITY

We made the Python scripts available, that can be used for extracting descriptors from the example data set [48].

ACKNOWLEDGEMENTS

We gratefully acknowledge funding from the Defense Advanced Research Projects Agency (Defense Sciences

Office) [Agreement No.: HR0011-16-2-0043]. We acknowledge funding from the National Science Foundation Harnessing the Data Revolution NSF-HDR-OAC-1940231. This work utilized the Summit supercomputer, which is supported by the National Science Foundation (awards ACI-1532235 and ACI-1532236), the University of Colorado Boulder, and Colorado State University. The Summit supercomputer is a joint effort of the University of Colorado Boulder and Colorado State University.

AUTHOR CONTRIBUTIONS

A.K.P contributed to the acquisition and the analysis of data and the creation of new scripts used in the study. S.N. contributed to the conception and the design of the work, the interpretation of data, drafting and revision of the article.

COMPETING INTERESTS

The authors declare no competing interests.

MATERIALS AND METHODS

Training and Test Structures for All ML Models

Training Structures: We consider ideal superlattices with both even and odd number of monolayers, referred to as $\text{Si}_{2p}\text{Ge}_{2p}$ ($p = 1, 2, \dots, 14$) and $\text{Si}_{2q-1}\text{Ge}_{2q-1}\text{Si}_{2q-1}\text{Ge}_{2q-1}$ ($q = 1, 2, \dots, 7$), respectively. The total number of atoms in model supercells (SCs) of these superlattices are even multiples of four. The SCs of $\text{Si}_{2p}\text{Ge}_{2p}$ configurations include $4p$ atoms and $\text{Si}_{2q-1}\text{Ge}_{2q-1}\text{Si}_{2q-1}\text{Ge}_{2q-1}$ configurations have $4(2q-1)$ atoms. We construct the SCs using a template that includes four atomic positions, as we discuss below. For the superlattices with odd number of monolayers, we double the SC sizes to account for the structure periodicity. We consider both strain symmetrized superlattices and superlattices with applied strains: 0.00%, 0.59%, 1.16%, 1.73%, and 2.31%. The strains are measured relative to bulk Si lattice constant: $((a' - a_{\text{Si}})/a_{\text{Si}}) \times 100$, where $a_{\text{Si}} = 5.47 \text{ \AA}$. The applied in-plane strain values correspond to alloy growth substrates, $\text{Si}_{1-x}\text{Ge}_x$, with varied Ge concentrations: $x = 0, 0.1, 0.2, 0.3, 0.4$.

Test Structures for Forward ML Model: Strain-symmetrized (i) $\text{Si}_8\text{Ge}_8\text{Si}_{20}\text{Ge}_{20}$ heterostructure and (ii) $\text{Si}_{28}\text{Ge}_{28}$ superlattice.

Test Structure for Reverse Learning CNN Model: Strain-symmetrized (i) $\text{Si}_8\text{Ge}_8\text{Si}_{20}\text{Ge}_{20}$ heterostructure, (ii) $\text{Si}_{28}\text{Ge}_{28}$ superlattice, (iii) relaxed and strained bulk Si models and (iv) ARPES images adopted from Ref. [44].

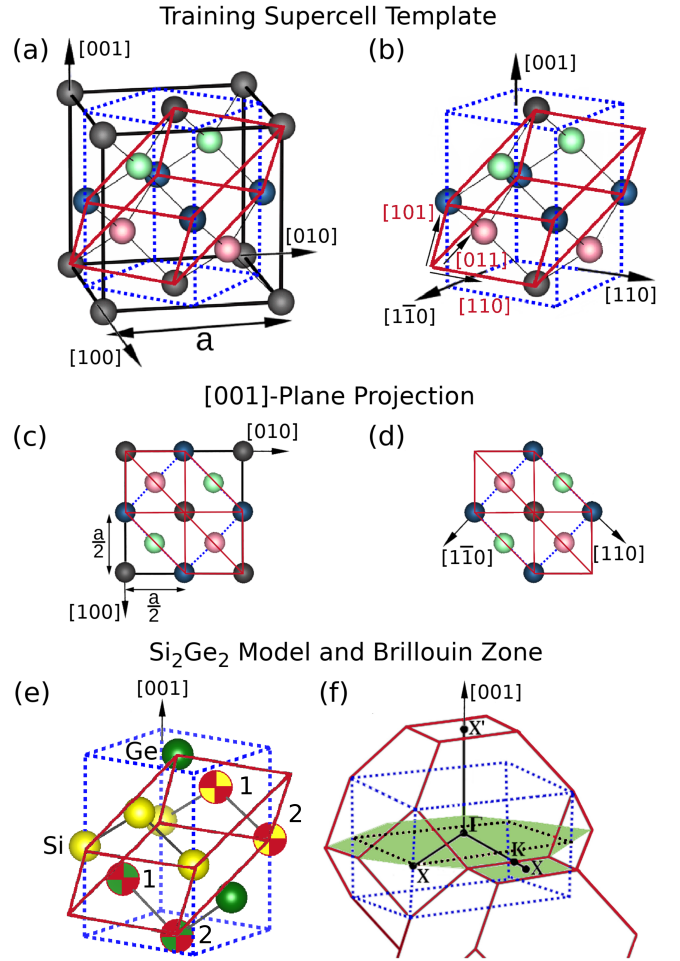


FIG. 8. **Generation of training supercells (SC) and selection of reference cells (RC):** (a, b) Tetragonal SC template (blue dashed lines) generated from a bulk Si conventional cell (black solid lines). a refers to bulk Si lattice constant. SC template includes four atomic positions, with one position per monolayer stacked along $[001]$ direction: black, red, blue and green. Representative two-atom RC chosen for unfolding (solid red lines). (c, d) Atomic positions in Si conventional cell, SC template and RC viewed along the $[001]$ direction. (e) Si_2Ge_2 superlattice SC, with two Si and two Ge atoms marked with red. Other atoms are replicas. Pairs of marked SC atoms ('1' and '2') are mapped to the two corresponding RC atomic positions, respectively. (f) SC (blue) and RC (red) Brillouin zone (BZ). Black dashed line represents projection of SC BZ onto the $[001]$ plane passing through Γ point. Symmetry points and paths in the green plane are used to obtain effective band structures or spectral functions.

Supercells: We generate the model SCs for all training and test superlattices and heterostructures, using a four-atom bulk Si tetragonal cell template (Si_4). The template is derived from a bulk Si cubic conventional cell. The template and the cubic cell are shown with blue dashed lines and black solid lines in Fig. 8(a, b), respectively. The volume of the template is half of the

volume of the cubic cell. The lattice parameters of the template are given by, $a' = b' = 2.73\text{\AA}$ and $c = 5.47\text{\AA}$, following geometry optimization. $c = 5.47\text{\AA}$ is same as lattice constant of bulk Si cubic cell. Our values agree with previous DFT results [49]. Although, it is known that the DFT-predicted lattice constants of bulk Si are $\sim 1\%$ higher than experimental values [50]. The basis vectors of the SC template are given by $a'[\bar{1}10]$, $b'[110]$, and $c[001]$. The template is periodically extended in the $[001]$ growth direction. The template can be used to span a bulk Si system with cubic symmetry, e.g., $[001]$ grown superlattices, by replicating in the $[110]$, $[\bar{1}10]$ and $[001]$ directions. This template allows us to investigate a large variety of superlattices and heterostructures, while keeping the computational expense at a minimum.

The template includes four atomic positions, see Fig. 8. The black, red, blue and green colors, represent atomic positions residing in planes that are $a/4$ apart along $[001]$. Fig. 8(c, d) shows the atomic positions as viewed along the $[001]$ direction. To create the superlattice models we insert Si and Ge atoms in the template atomic positions. For example, we obtain a Si_2Ge_2 superlattice model by inserting Si atoms in the blue and green positions, and Ge atoms in the black and red positions of the template, respectively (Fig. 8(e)). The red '+' symbols show the two Si and the two Ge atoms, while the replicas are unmarked. We obtain strain-symmetrized or strained configurations by performing geometry optimization of the supercell models. To create superlattice models with longer periods, we start with $[001]$ periodically replicated models of SC template. We insert Si and Ge atoms in the atomic positions of the replicated template. That way, the resulting SC includes the desired number of Si and Ge monolayers. A representative eight-atom Si_4Ge_4 superlattice model is shown in Fig. 1(b). Table 1 of Supplementary Materials lists the lattice parameters of all geometry optimized supercells studied in this article.

Test Structures for Combined Model: Strain-symmetrized and strained bulk Si, modeled with Si_4 SC. The strained model is considered to be grown on $\text{Si}_{0.7}\text{Ge}_{0.3}$ substrate, with 1.73% in-plane strain.

Test ARPES Image for Combined Model: ARPES spectra adopted from Fig. 6.2 of Ref. 44. We combine the band dispersions along $\Gamma - X$ (Fig. 6.2(a)) and $\Gamma - K - X$ paths (Fig. 6.2(c)) into a single image. We interpolate the experimental images from the resolution provided in Ref. [44] to 64×64 pixels in size and for energy range from -6 eV to 0 eV.

DFT Computation Details

We optimize the lattice constants and the atomic positions of training and test SC models with conjugate gradient algorithm [51]. We sample the SC BZ with $11 \times 11 \times 11$ k -point mesh, generated by the Monkhorst-

Pack scheme [52]. Although c is generally larger than a' and b' , we use $11 \times 11 \times 11$ k -point mesh to accommodate for ample sampling along $[001]$. Such sampling is particularly necessary for complex heterostructures with irregularly thick Si or Ge layers. To simulate SC under applied strain, we assign a' and b' to be equal to the substrate lattice constants and relax the cell shape in the cross-plane $[001]$ direction. The DFT calculations reported in this article, are performed using the OpenMX code which is based on norm-conserving pseudopotentials generated with multiple reference energies [53] and linear combination of optimized pseudoatomic basis functions [33]. We use the Perdew-Burke-Ernzenhof exchange-correlation formulation [37] of the generalized gradient approximation. Self-consistent field (SCF) calculations are performed during the geometry optimization with energy convergence threshold set to 10^{-9} Hartree. The SCs are optimized until the maximum force on an atom became less than 10^{-4} Hartree Bohr $^{-1}$. We use a regular mesh of 200 Ryd in real space for the numerical integrations and solution of Poisson equation [54]. We do not include spin-orbit interaction in our analysis since strain induced band splittings were shown to be larger than the spin-orbit splittings [16]. For the silicon and germanium atoms, 2, 2, and 1 optimized radial functions were allocated for the s-, p- and d-orbitals, respectively, as denoted by s2p2d1. The one-particle wave functions are expressed by the linear combination of pseudo-atomic orbital (PAO) basis functions centered on atomic site [33, 34]. A cutoff radius of 7.0 Bohr was used for all the basis functions. Following relaxation, we perform non self-consistent field (NSCF) calculations using the linear combinations of atomic orbitals (LCAO) pseudopotential method [33, 34]. We obtain the eigenstates, $|KJ\rangle$ and energy, ϵ_{KJ} , for the range from -10 eV to 10 eV. Here, $|KJ\rangle$ represents a Bloch state with crystal momentum K and band index J , ϵ_{KJ} is the corresponding eigenvalue [55]. We use a $7 \times 7 \times 7$ k -point mesh generated according to the Monkhorst-Pack method [52] to sample the supercell BZ. Such k -point mesh has been used in DFT studies for calculation of electronic structure of two-atom Si lattice [55].

Supercells and Reference Cells

We unfold SC electronic band structures to the BZ of chosen reference cells (RCs) via SFs [6–9, 12, 56]. Figure 8 (a-d) show a representative rhombohedron RC with red solid lines. The embedding cubic conventional cell and the SC template are shown with black solid lines and blue dashed lines, respectively. The volume of the RC is $1/4$ the volume of the conventional cell. The RC resembles the two-atom primitive cell of FCC Si lattice. If no symmetry breaker is present in the SC, the RC will be identical to a primitive cell. We determine the RC

basis vectors from SC basis vectors. In general, the SC basis vectors are given by:

$$\vec{B} = \begin{pmatrix} a' & -a' & 0 \\ b' & b' & 0 \\ 0 & 0 & c' \end{pmatrix}, \quad (4)$$

where $a' = b'$ and c' are the SC lattice parameters. We show the a', b' and c' for different superlattices or heterostructures, in Table 1 of Supplementary Materials. The SC (\vec{B}) and the RC basis vectors (\vec{b}) are related via a transformation matrix, M : $\vec{b} = M\vec{B}$, with M given by

$$M = \begin{pmatrix} -\frac{1}{2} & \frac{1}{2} & \frac{1}{2N} \\ \frac{1}{2} & \frac{1}{2} & \frac{1}{2N} \\ 0 & 1 & 0 \end{pmatrix}, \quad (5)$$

where N represents number of templates stacked along [001] direction in the supercell. N is equal to the total number of atoms in the SC divided by 4. For example, $N = 1$ for Si_2Ge_2 , and $N = 2$ for Si_4Ge_4 and so on. Thus, the RC basis vectors are given by:

$$\vec{b} = \begin{pmatrix} \frac{b'-a'}{2} & \frac{b'+a'}{2} & \frac{c'}{2N} \\ \frac{b'+a'}{2} & \frac{b'-a'}{2} & \frac{c'}{2N} \\ \frac{b'}{2} & \frac{b'}{2} & 0 \end{pmatrix}. \quad (6)$$

We obtain different basis vectors for the corresponding two-atom RCs, from the SC basis vectors a', b' and c' , shown in Table 1 of Supplementary Materials. Fig. 8(e) shows the RC of a Si_2Ge_2 SC and Fig. 8(f) shows the corresponding BZ. We compute ASF of atoms along the path indicated by the green plane, and generate training data.

Spectral Weights and Spectral Functions

The steps for computing SFs are as follows:

- (i) Geometry optimization of chosen SCs;
- (ii) Calculating SC eigenstates for a k -point mesh;
- (iii) Identifying RC and a set of wave vectors $\{k_i\}$ along a chosen path in the respective BZ;
- (iv) Computing SFs for each atom along the path;
- (v) Repeating steps (i)–(iv) for a different SC;

Below we discuss the approach used for step (iv).

In the LCAO method, a Bloch state $|KJ\rangle$ is expanded in the form of a linear combination of atomic basis functions, $|RN\rangle$, as

$$|KJ\rangle = \sum_N C_N^{KJ} |KN\rangle, \quad (7)$$

while,

$$|KN\rangle = \frac{1}{\sqrt{L}} \sum_R e^{i\mathbf{K}\cdot\mathbf{R}} |RN\rangle. \quad (8)$$

Here, C_N^{KJ} are the LCAO coefficients. The atomic basis functions, $|RN\rangle$, are placed in every unit cell and specified with a translational lattice vector R . N represents a symbolic orbital index, that consists of the atomic position relative to R , a multiplicity index for radial functions, an angular momentum quantum number, and a magnetic quantum number. L is the number of unit cells included in the Born-von Karman boundary condition. We unfold the SC band structures to RC BZs via SFs, $\hat{A}(E)$, following the method proposed in Ref. [9]. It can be shown that the SF expressions in the SC and the RC representations are related via

$$\begin{aligned} & A_{kj,kj}(E) \\ &= \sum_{mnK} S_{mn}^{-1}(k) \langle kn|KJ\rangle A_{KJ,KJ}(E) \langle KJ|km\rangle. \end{aligned} \quad (9)$$

Here, $|kj\rangle$ is a Bloch state and m and n represent symbolic orbital indices in the RC representations. $S_{mn}(k)$ are the overlap matrix elements. The spectral function, $A_{kj,kj}(E)$, can be represented as a linear combination of unfolded spectral weights, W_{KJ}^k [9]:

$$A_{kj,kj}(E) = \sum_K W_{KJ}^k A_{KJ,KJ}(E) \quad (10)$$

with

$$\begin{aligned} W_{KJ}^k &= \frac{L}{l} \sum_G \delta_{k-G,K} \\ &\times \sum_{MNr} e^{i\mathbf{k}\cdot(\mathbf{r}-\mathbf{r}'(M))} C_M^{KJ} C_N^{KJ*} S_{0N,rm(M)}. \end{aligned} \quad (11)$$

Here, L and l are the number of unit cells in SC and RC, respectively. $r'(M)$ and $m(M)$ refer to lattice vectors and orbital indices of the RC atomic basis, respectively, that correspond to the SC symbolic orbital index M . The delta function, $\delta_{k-G,K}$ signifies that W at k is contributed only by the folded Bloch state with $k - G = K$, where G is a reciprocal lattice vector. The spectral weights are determined by the phase factor $e^{i\mathbf{k}\cdot(\mathbf{r}-\mathbf{r}'(M))}$, LCAO coefficients, C_M^{KJ} or C_N^{KJ} , and overlap matrix elements, $S_{0N,rm(M)}$. In the LCAO method, we allocate same basis functions for each atomic species in the SCs with varied periods and compositions. However, same AOs contribute differently to the electronic bands of different SCs due to structural features. The influence of atomic structures is recorded in the LCAO coefficients and the overlap integrals between basis functions. It is important to note that the spectral weights are calculated in the SC representation without relying on any RC details. Thus, unfolding is performed purely in a mathematical sense and is valid as long as a RC can be defined.

Additionally, we compute the atomically resolved SFs that allow us to analyze how spectral weights vary based

on the atomic environment. To obtain ASFs, we express the orbitally resolved SFs as:

$$A_{k_j, k_j}^M(E) = \sum_K A_{KJ, KJ}(E) W_{KJM}^k, \quad (12)$$

where, the orbitally resolved spectral weights, W_{KJM}^k , are given by

$$W_{KJM}^k = \frac{L}{l} \sum_G \delta_{k-G, K} C_M^{KJ} \times \sum_{Nr} e^{i\mathbf{k} \cdot (\mathbf{r} - \mathbf{r}'(M))} C_N^{KJ*} S_{0N, rm(M)}, \quad (13)$$

and are obtained by rearranging Eq. 11. Equation 10 can then be written as:

$$A_{k_j, k_j}(E) = \sum_M A_{k_j, k_j}^M(E) = \sum_K A_{KJ, KJ}(E) \sum_M W_{KJM}^k. \quad (14)$$

The values of index M depend on the SC size and the number of basis functions for each atom. As an example, for a supercell with n atoms and m basis function per atom, M ranges from 1 to $n \times m$. By decomposing the spectral weights and the SFs, it is possible to analyze the contribution from different localized basis functions to bands. We obtain the atomically resolved SFs from the orbitally resolved SFs. Considering that there are m basis functions assigned to the p^{th} atom in the supercell: $\{p_1, \dots, p_m\} \subset M$, we add p_m orbitally resolved spectral weights, $W_{KJp_m}^k$, to obtain the ASFs for each atom. Thus, total SF can then be written as:

$$A_{k_j, k_j}(E) = \sum_K A_{KJ, KJ}(E) \sum_p \sum_{m \subset M} W_{KJp_m}^k, \quad (15)$$

or, in terms of the atomically resolved SFs, $A_{k_j, k_j}^p(E)$,

$$A_{k_j, k_j}(E) = \sum_p A_{k_j, k_j}^p(E) = \sum_p \sum_{m \subset M} A_{k_j, k_j}^{p_m}(E). \quad (16)$$

Here, $A_{KJ, KJ}(E)$ is a delta function, $\delta(E - \epsilon_{KJ})$.

We obtain the SC eigenstates (ϵ_{KJ}) for the energy range from -10 eV to 10 eV from the NSCF calculations. We compute spectral weights by unfolding the SC eigenstates, $|KJ\rangle$, on RC Bloch states $|k_i j\rangle$. We choose a set of 100 wave vectors $\{k_i\}$ along the $X - \Gamma - K - X$ path of the RC Brillouin zone (as depicted in Fig. 8(f)). We do not explicitly keep track of the band indices and drop the subscript j . The spectral weights are then convoluted with the above delta function to obtain $A_{k, k}^p(E)$ or $A^p(k, E)$. We model the delta function $\delta(E - \epsilon_{KJ})$ representing $A_{KJ, KJ}(E)$ with an exponential function with width 0.02 eV. For the forward ML model, we use a 450 point sampling for the delta function between $-6 \text{ eV} \leq E \leq 3 \text{ eV}$. We then interpolate over 300×450 values of $A^p(k, E)$ and obtain 64×96 ASF values. The ASFs, $A^p(k, E)$, are defined over $\{k\} \rightarrow X - \Gamma - K - X$ and $-6 \text{ eV} \leq E \leq 3$

eV. The total SFs, $A(k, E)$, are obtained by summing over $A^p(k, E)$ for all atoms in the superlattice or heterostructure. $A(k, E)$'s are also defined over the same k and E range, with a 64×96 sampling. In the last part of this study, while comparing with the ARPES spectra, we use a 300 point sampling for $-6 \text{ eV} \leq E \leq 0 \text{ eV}$, using 0.02 eV wide delta-function. We choose 300 $\{k_i\}$ vectors along $X - \Gamma - K - X$ to keep a square grid for (k, E) .

ML Model Implementations

Forward Learning Approach: We implement the forward learning approach using NN and RF model, separately. **NN model:** The model has three fully-connected (dense) layers represented by the rows. The input layer with 9 input parameters is followed by two hidden layers with 16 and 32 nodes, respectively. Rectified Linear Unit (ReLU) activation functions are implemented for the the hidden layers. The number of input parameters is equal to number of features considered, nine in our case as shown in Table 1. The output layer has 6144 nodes and linear activation function. The number of nodes in the output layer corresponds to the $64 \times 96 = 6144$ interpolated $A^p(k, E)$ values for the respective superlattice or heterostructure. The same NN model architecture can be employed even when the size of input or output data is changed. Table 4 of Supplementary Materials shows the layers, the number of nodes in each layer and the activation functions of the NN model. We allocate 20% of training data for model validation. We sample random batches of size 32 sequentially from the training set (e.g., 32/3360) at each epoch during training. The last batch will be of size less than 32 if the remainder is not zero. We update the weights iteratively for 5000 epochs till MAE between predicted and validation ASF:

$$MAE(A^p, \hat{A}^p) = \frac{\sum_{k, E} |A^p(k, E) - \hat{A}^p(k, E)|}{64 \times 96}, \quad (17)$$

reaches a minimum. We employ the ADAM stochastic optimization method for gradient descent [57] with learning rate of 0.0005 to minimize the loss function, MAE in this case. The high-level NNs are implemented using the Python Keras library [58]. The optimized weights are used to predict ASF values for test structures.

RF model: The RF model assembles results of several decision trees. Each tree is built from a random selection of training data that include both structural features and ASF of training superlattices. We use feature based decision rules to partition the training data into subsets. As an example, decision rule could be based on order parameter values, e.g., $Q^{x,1}$ in the range 0.5 – 0.6, representing different atomic environments. Training data with $Q^{x,1}$ in the range 0.5 – 0.6 could form a subset. The branches of the trees are constituted from the decision rules that identify features that minimize the in-

trasubset variation of ASF. ASF that maximizes fitting over the subset data are assigned as leaves of the tree. The tree generation process is then repeated for other random subsets of training data. We average over the predicted $A^p(k, E)$ from all the trees to obtain the final predictions. We implement the RF module available in the scikit-learn Python package [59]. We use 200 regression trees per ensemble and default values for all other parameters recommended for the package. We use input and output same as the NN model, as listed in Table 4 of Supplementary Materials.

Reverse Learning Approach: We implement the reverse learning approach using CNN model. CNN model is extensively used for feature extraction in digital images and is able to assemble complex patterns from small training data [60]. We employ CNN to identify patterns in the training images of ASFs. The patterns of ASF images represent effects of translational symmetry breaking on the electronic bands of heterostructures. We use the CNN model to learn the relationships between these patterns and the descriptors. The details of the model are shown in Table 5 of Supplementary Materials. The model includes one coordinate channel layer (Coordinate-Channel2D) [61] and three convolution layers (Conv2D), with 8, 16, and 32 filters each. Each convolution layers is followed by a max pooling layer (MaxPooling2D) and batch normalization. The dimension of the tensor at the input layer is (64, 64, 1), where the first two are the pixel dimensions of the image, and the third is the number of channels in the input image. The 64×64 pixels of $A^p(k, E)$ images are provided as input. Two fully connected layers (Dense) with 16 and 32 nodes respectively with ReLU activation functions are followed by an output layer (Dense) with linear activation function. The set of descriptors outlined above are passed through the output layer.

We consider 13 different Fermi level alignments. We shift the mid-gap DFT zero energy level of the SFs of each configurations by a value dE in the range from -0.5 eV to +0.5 eV with a step of 1/13 eV. The alignments serve a role of electron doping level in ARPES experiments. This training helps the model to predict the descriptors of ARPES images with different Fermi level alignments. We allocate 20% of training data for model validation. We sample random batches of size 32 sequentially from the training set at each epoch during training. We employ the ADAM stochastic optimization method for gradient descent [57] with learning rate of 0.0005 to minimize the loss function. We update the weights iteratively for 2000 epochs till the MAE between predicted and validation descriptors reaches a minimum.

Combined Forward-Reverse Learning Model: Finally, we merge the forward and reverse trained ML models shown in Tables 4 and 5 of Supplementary Materials, respectively, into one combined model.

* sanghamitra.neogi@colorado.edu

- [1] Alferov, Z. I. Nobel lecture: The double heterostructure concept and its applications in physics, electronics, and technology. *Rev. Mod. Phys.* **73**, 767 (2001).
- [2] Paul, D. J. Si/SiGe heterostructures: from material and physics to devices and circuits. *Semicond. Sci. Technol.* **19**, R75 (2004).
- [3] David, T. *et al.* New strategies for producing defect free sige strained nanolayers. *Scientific reports* **8**, 1–10 (2018).
- [4] Chen, P. *et al.* Role of surface-segregation-driven intermixing on the thermal transport through planar si/ge superlattices. *Physical review letters* **111**, 115901 (2013).
- [5] Ku, W., Berlijn, T., Lee, C.-C. *et al.* Unfolding first-principles band structures. *Physical review letters* **104**, 216401 (2010).
- [6] Popescu, V. & Zunger, A. Extracting E versus k effective band structure from supercell calculations on alloys and impurities. *Physical Review B* **85**, 085201 (2012).
- [7] Boykin, T. B., Kharche, N. & Klimeck, G. Brillouin-zone unfolding of perfect supercells having nonequivalent primitive cells illustrated with a si/ ge tight-binding parameterization. *Physical Review B* **76**, 035310 (2007).
- [8] Boykin, T. B., Kharche, N. & Klimeck, G. Non-primitive rectangular cells for tight-binding electronic structure calculations. *Physica E: Low-dimensional Systems and Nanostructures* **41**, 490–494 (2009).
- [9] Lee, C.-C., Yamada-Takamura, Y. & Ozaki, T. Unfolding method for first-principles LCAO electronic structure calculations. *Journal of Physics: Condensed Matter* **25**, 345501 (2013).
- [10] Chen, M. & Weinert, M. Layer k-projection and unfolding electronic bands at interfaces. *Physical Review B* **98**, 245421 (2018).
- [11] Popescu, V. & Zunger, A. Effective band structure of random alloys. *Physical review letters* **104**, 236403 (2010).
- [12] Boykin, T. B., Kharche, N., Klimeck, G. & Korkusinski, M. Approximate bandstructures of semiconductor alloys from tight-binding supercell calculations. *J. Phys.: Condens. Matter* **19**, 036203 (2007).
- [13] d’Avezac, M., Luo, J.-W., Chanier, T. & Zunger, A. Genetic-algorithm discovery of a direct-gap and optically allowed superstructure from indirect-gap si and ge semiconductors. *Physical review letters* **108**, 027401 (2012).
- [14] Zhang, L., Luo, J.-W., Saraiva, A., Koiller, B. & Zunger, A. Genetic design of enhanced valley splitting towards a spin qubit in silicon. *Nature communications* **4**, 1–7 (2013).
- [15] Satpathy, S., Martin, R. M. & Van de Walle, C. G. Electronic properties of the (100)(si)/(ge) strained-layer superlattices. *Physical Review B* **38**, 13237 (1988).
- [16] Hybertsen, M. S. & Schlüter, M. Theory of optical transitions in si/ge (001) strained-layer superlattices. *Physical Review B* **36**, 9683 (1987).
- [17] Tserbak, C., Polatoglou, H. & Theodorou, G. Unified approach to the electronic structure of strained si/ge superlattices. *Physical Review B* **47**, 7104 (1993).
- [18] Proshchenko, V. S., Dholabhai, P. P., Sterling, T. C. & Neogi, S. Heat and charge transport in bulk semiconductors with interstitial defects. *Physical Review B* **99**, 014207 (2019).
- [19] Proshchenko, V. S., Settipalli, M. & Neogi, S. Optimiza-

- tion of seebeck coefficients of strain-symmetrized semiconductor heterostructures. *Applied Physics Letters* **115**, 211602 (2019).
- [20] Proshchenko, V. S., Settipalli, M., Pimachev, A. K. & Neogi, S. Role of substrate strain to tune energy bands-seebeck relationship in semiconductor heterostructures. *Journal of Applied Physics* **129**, 025301 (2021).
- [21] Settipalli, M. & Neogi, S. Theoretical prediction of enhanced thermopower in n-doped si/ge superlattices using effective mass approximation. *J. Electron. Mater.* **49**, 4431–4442 (2020).
- [22] Pimachev, A. K. & Neogi, S. First-principles prediction of electronic transport in fabricated semiconductor heterostructures via physics-aware machine learning. *npj Computational Materials* **7**, 93 (2021).
- [23] Settipalli, M., Proshchenko, V. S. & Neogi, S. The effect of electron-phonon and electron-impurity scattering on the electronic transport properties of silicon/germanium superlattices. *Journal of Materials Chemistry C* **10**, 7525–7542 (2022).
- [24] Ward, L. *et al.* Including crystal structure attributes in machine learning models of formation energies via voronoi tessellations. *Physical Review B* **96**, 024104 (2017).
- [25] Ghiringhelli, L. M., Vybiral, J., Levchenko, S. V., Draxl, C. & Scheffler, M. Big data of materials science: critical role of the descriptor. *Phys. Rev. Lett.* **114**, 105503 (2015).
- [26] Schäffler, F. High-mobility si and ge structures. *Semiconductor Science and Technology* **12**, 1515 (1997).
- [27] Cowley, J. An approximate theory of order in alloys. *Physical Review* **77**, 669 (1950).
- [28] Xie, T. & Grossman, J. C. Crystal graph convolutional neural networks for an accurate and interpretable prediction of material properties. *Physical review letters* **120**, 145301 (2018).
- [29] Choudhary, K. & DeCost, B. Atomistic line graph neural network for improved materials property predictions. *npj Computational Materials* **7**, 185 (2021).
- [30] Gupta, V. *et al.* Structure-aware graph neural network based deep transfer learning framework for enhanced predictive analytics on diverse materials datasets. *npj Computational Materials* **10**, 1 (2024).
- [31] Jain, A. *et al.* Commentary: The materials project: A materials genome approach to accelerating materials innovation. *APL materials* **1** (2013).
- [32] Choudhary, K. *et al.* The joint automated repository for various integrated simulations (jarvis) for data-driven materials design. *npj computational materials* **6**, 173 (2020).
- [33] Ozaki, T. Variationally optimized atomic orbitals for large-scale electronic structures. *Physical Review B* **67**, 155108 (2003).
- [34] Ozaki, T. & Kino, H. Numerical atomic basis orbitals from h to kr. *Physical Review B* **69**, 195113 (2004).
- [35] Ozaki, T. & Kino, H. Efficient projector expansion for the ab initio lcao method. *Physical Review B* **72**, 045121 (2005).
- [36] Ozaki, T. *et al.* www.openmx-square.org (2013). URL <http://www.openmx-square.org/>.
- [37] Perdew, J. P., Burke, K. & Ernzerhof, M. Generalized gradient approximation made simple. *Physical review letters* **77**, 3865 (1996).
- [38] Yu, D., Zhang, Y. & Liu, F. First-principles study of electronic properties of biaxially strained silicon: Effects on charge carrier mobility. *Physical Review B* **78**, 245204 (2008).
- [39] Hinsche, N. F., Mertig, I. & Zahn, P. Effect of strain on the thermoelectric properties of silicon: an ab initio study. *Journal of Physics: Condensed Matter* **23**, 295502 (2011).
- [40] Hinsche, N., Mertig, I. & Zahn, P. Thermoelectric transport in strained si and si/ge heterostructures. *Journal of Physics: Condensed Matter* **24**, 275501 (2012).
- [41] Eales, T. D. *et al.* Ge1-xsnx alloys: consequences of band mixing effects for the evolution of the band gap γ -character with sn concentration. *Scientific reports* **9**, 1–10 (2019).
- [42] Froyen, S., Wood, D. & Zunger, A. Structural and electronic properties of epitaxial thin-layer si n ge n superlattices. *Physical Review B* **37**, 6893 (1988).
- [43] Seo, H. *et al.* Critical differences in the surface electronic structure of ge (001) and si (001): Ab initio theory and angle-resolved photoemission spectroscopy. *Physical Review B* **89**, 115318 (2014).
- [44] Constantinou, P. C. *Fabrication and characterization of metallic, two-dimensional dopant δ -layers in silicon.* Ph.D. thesis, UCL (University College London) (2021).
- [45] Strocob, V. N. *et al.* k-resolved electronic structure of buried heterostructure and impurity systems by soft-x-ray arpes. *Journal of Electron Spectroscopy and Related Phenomena* **236**, 1–8 (2019).
- [46] Leonardi, A., Leoni, M., Li, M. & Scardi, P. Strain in atomistic models of nanocrystalline clusters. *Journal of Nanoscience and Nanotechnology* **12**, 8546–8553 (2012).
- [47] Garg, P. & Rupert, T. J. Grain incompatibility determines the local structure of amorphous grain boundary complexions. *Acta Materialia* **244**, 118599 (2023).
- [48] Cuantam lab - github page. <https://github.com/CUANTAM>.
- [49] Wright, A. Density-functional-theory calculations for the silicon vacancy. *Physical Review B* **74**, 165116 (2006).
- [50] Semiconductor, V. *General Properties of Si, Ge, SiGe, SiO₂ and Si₃N₄* (2002).
- [51] Press, W. H., Teukolsky, S. A., Vetterling, W. T. & Flannery, B. P. *Numerical Recipes in Fortran 90: Numerical recipes in Fortran 77V. 2. Numerical recipes in Fortran 90* (Cambridge University Press, 1996).
- [52] Monkhorst, H. J. & Pack, J. D. Special points for brillouin-zone integrations. *Physical review B* **13**, 5188 (1976).
- [53] Morrison, I., Bylander, D. & Kleinman, L. Nonlocal hermitian norm-conserving vanderbilt pseudopotential. *Physical Review B* **47**, 6728 (1993).
- [54] Soler, J. M. *et al.* The siesta method for ab initio order-n materials simulation. *Journal of Physics: Condensed Matter* **14**, 2745 (2002).
- [55] Bystrom, K., Broberg, D., Dwaraknath, S., Persson, K. A. & Asta, M. Pawpyseed: Perturbation-extrapolation band shifting corrections for point defect calculations. *arXiv preprint arXiv:1904.11572* (2019).
- [56] Lee, Y.-T., Lee, C.-C., Fukuda, M. & Ozaki, T. Unfolding optical transition weights of impurity materials for first-principles LCAO electronic structure calculations. *Physical Review B* **102**, 075143 (2020).
- [57] Kingma, D. P. & Ba, J. Adam: A method for stochastic optimization. *arXiv preprint arXiv:1412.6980* (2014).
- [58] Chollet, F. *et al.* Keras (2015). URL <https://github.com>.

com/fchollet/keras.

- [59] Pedregosa, F. *et al.* Scikit-learn: Machine learning in python. *Journal of machine learning research* **12**, 2825–2830 (2011).
- [60] Sharma, A., Vans, E., Shigemizu, D., Boroevich, K. A. & Tsunoda, T. Deepinsight: A methodology to transform a non-image data to an image for convolution neural network architecture. *Scientific reports* **9**, 1–7 (2019).
- [61] Liu, R. *et al.* An intriguing failing of convolutional neural networks and the coordconv solution. *Advances in neural information processing systems* **31** (2018).
- [62] Niquet, Y.-M., Rideau, D., Tavernier, C., Jaouen, H. & Blase, X. Onsite matrix elements of the tight-binding hamiltonian of a strained crystal: Application to silicon, germanium, and their alloys. *Physical Review B* **79**, 245201 (2009).
- [63] Perdew, J. P. Density functional theory and the band gap problem. *International Journal of Quantum Chemistry* **30**, 451–451 (1986).
- [64] Perdew, J. P. *et al.* Understanding band gaps of solids in generalized kohn–sham theory. *Proceedings of the National Academy of Sciences* **114**, 2801–2806 (2017).
- [65] Morales-García, Á., Valero, R. & Illas, F. An empirical, yet practical way to predict the band gap in solids by using density functional band structure calculations. *The Journal of Physical Chemistry C* **121**, 18862–18866 (2017).
- [66] Heyd, J., Scuseria, G. E. & Ernzerhof, M. Hybrid functionals based on a screened coulomb potential. *Journal of chemical physics* **118**, 8207–8215 (2003).
- [67] Hummer, K., Harl, J. & Kresse, G. Heyd-scuseria-ernzerhof hybrid functional for calculating the lattice dynamics of semiconductors. *Physical Review B* **80**, 115205 (2009).
- [68] Stephenson, C. *et al.* Band structure of germanium carbides for direct bandgap silicon photonics. *Journal of Applied Physics* **120**, 053102 (2016).

SUPPLEMENTARY MATERIALS

LATTICE PARAMETERS OF TRAINING AND TEST SUPERCELLS

Table 3 lists the lattice parameters of all geometry optimized supercells investigated in this article.

DESCRIPTORS OF REPRESENTATIVE SUPERLATTICE

Table 4 shows example values of atomic environment descriptors (atom type and structural descriptors) of Si_5Ge_3 superlattice. As can be seen from the table, the descriptors along the x and y directions, (b_x, b_y) and (Q_x^1, Q_y^1) , are identical for all atoms. We only show the pairs of the first order parameters, (Q_x^1, Q_y^1) , for brevity, however, the same is true for (Q_x^2, Q_y^2) and (Q_x^3, Q_y^3) .

TABLE 3. Lattice Parameters of Supercells, Å; Basis vectors: $a'[1\bar{1}0]$, $a'[110]$, $c'[001]$

| Structures | Strain-Symmetrized | | Grown on $\text{Si}_{1-x}\text{Ge}_x$, $x =$ | | | | |
|------------------------------------|--------------------|-------|---|-------|-------|-------|-------|
| | a' | c' | 0.0 | 0.1 | 0.2 | 0.3 | 0.4 |
| Si_4 | 2.73 | 5.47 | 5.47 | 5.41 | 5.35 | 5.29 | 5.23 |
| Ge_4 | 2.89 | 5.79 | 6.48 | 6.40 | 6.33 | 6.26 | 6.19 |
| $(\text{Si}_1\text{Ge}_1)^2$ | 2.81 | 5.60 | 5.93 | 5.86 | 5.80 | 5.73 | 5.67 |
| Si_2Ge_2 | 2.81 | 5.60 | 5.93 | 5.86 | 5.79 | 5.73 | 5.66 |
| $(\text{Si}_3\text{Ge}_3)^2$ | 2.81 | 16.86 | 17.79 | 17.59 | 17.39 | 17.19 | 16.99 |
| Si_4Ge_4 | 2.81 | 11.25 | 11.87 | 11.73 | 11.60 | 11.47 | 11.34 |
| $(\text{Si}_5\text{Ge}_5)^2$ | 2.81 | 28.12 | 29.66 | 29.32 | 28.98 | 28.66 | 28.33 |
| Si_6Ge_6 | 2.81 | 16.88 | 17.82 | 17.61 | 17.41 | 17.21 | 17.02 |
| $(\text{Si}_7\text{Ge}_7)^2$ | 2.81 | 39.39 | 41.55 | 41.08 | 40.61 | 40.15 | 39.70 |
| Si_8Ge_8 | 2.81 | 22.53 | 23.75 | 23.48 | 23.21 | 22.95 | 22.69 |
| $(\text{Si}_9\text{Ge}_9)^2$ | 2.81 | 50.63 | 53.44 | 52.83 | 52.22 | 51.63 | 51.05 |
| $\text{Si}_{10}\text{Ge}_{10}$ | 2.81 | 28.15 | 29.72 | 29.38 | 29.04 | 28.71 | 28.39 |
| $(\text{Si}_{11}\text{Ge}_{11})^2$ | 2.81 | 61.90 | 65.37 | 64.62 | 63.89 | 63.16 | 62.45 |
| $\text{Si}_{12}\text{Ge}_{12}$ | 2.81 | 33.75 | 35.65 | 35.24 | 34.84 | 34.44 | 34.05 |
| $(\text{Si}_{13}\text{Ge}_{13})^2$ | 2.81 | 73.10 | 77.14 | 76.26 | 75.39 | 74.53 | 73.69 |
| $\text{Si}_{14}\text{Ge}_{14}$ | 2.81 | 39.39 | 41.55 | 41.07 | 40.61 | 40.15 | 39.69 |
| $\text{Si}_{16}\text{Ge}_{16}$ | 2.81 | 45.01 | 47.51 | 46.96 | 46.43 | 45.90 | 45.38 |
| $\text{Si}_{18}\text{Ge}_{18}$ | 2.81 | 50.65 | 53.47 | 52.86 | 52.26 | 51.67 | 51.08 |
| $\text{Si}_{20}\text{Ge}_{20}$ | 2.81 | 56.29 | 59.46 | 58.78 | 58.11 | 57.45 | 56.80 |
| $\text{Si}_{22}\text{Ge}_{22}$ | 2.81 | 61.88 | 65.27 | 64.52 | 63.78 | 63.06 | 62.35 |
| $\text{Si}_{24}\text{Ge}_{24}$ | 2.81 | 67.55 | 71.26 | 70.44 | 69.64 | 68.85 | 68.07 |
| $\text{Si}_{26}\text{Ge}_{26}$ | 2.81 | 73.15 | 77.23 | 76.34 | 75.47 | 74.61 | 73.77 |
| $\text{Si}_{28}\text{Ge}_{28}$ | 2.81 | 78.79 | 83.20 | 82.25 | 81.31 | 80.39 | 79.48 |
| HS | 2.79 | 79.65 | | | | | |
| | | | substrate tuned a' | | | | |
| | | | 2.73 | 2.75 | 2.76 | 2.78 | 2.80 |

$(\text{Si}_q\text{Ge}_q)^2 \equiv \text{Si}_q\text{Ge}_q\text{Si}_q\text{Ge}_q$ for odd $q = 1, 3, 5, 7, 9, 11, 13$
 HS: $\text{Si}_8\text{Ge}_8\text{Si}_{20}\text{Ge}_{20}$

TABLE 4. Descriptors of Atoms of Si_5Ge_3 Superlattice

| Atom | Type | b_x | b_y | b_z | Q_x^1 | Q_y^1 | Q_z^1 | Q_x^2 | Q_z^2 | Q_x^3 | Q_z^3 | |
|---------------|------|-------|-------|-------|---------|---------|---------|---------|---------|---------|---------|------|
| Si | 1 | 2.617 | 2.617 | 2.625 | 0.55 | 0.55 | 0.51 | 0.49 | 0.47 | 0.38 | 0.37 | |
| Si | 1 | 2.589 | 2.589 | 2.626 | 0.96 | 0.96 | 0.92 | 0.68 | 0.64 | 0.56 | 0.52 | |
| Si_5 | Si | 1 | 2.592 | 2.592 | 2.632 | 0.99 | 0.99 | 1.00 | 0.89 | 0.83 | 0.56 | 0.51 |
| | Si | 1 | 2.589 | 2.589 | 2.626 | 0.96 | 0.96 | 0.92 | 0.68 | 0.64 | 0.56 | 0.52 |
| | Si | 1 | 2.617 | 2.617 | 2.625 | 0.55 | 0.55 | 0.51 | 0.49 | 0.47 | 0.39 | 0.37 |
| Ge_3 | Ge | 0 | 2.682 | 2.682 | 2.639 | 0.54 | 0.54 | 0.49 | 0.44 | 0.41 | 0.21 | 0.15 |
| | Ge | 0 | 2.716 | 2.716 | 2.647 | 0.95 | 0.95 | 0.89 | 0.42 | 0.30 | 0.27 | 0.24 |
| | Ge | 0 | 2.682 | 2.682 | 2.639 | 0.54 | 0.54 | 0.49 | 0.44 | 0.41 | 0.21 | 0.15 |

SUPERCELL BANDS OF REPRESENTATIVE SUPERLATTICE

Figure 9 shows supercell bands of (a) Si_2Ge_2 and (b) Si_4Ge_4 superlattices, respectively. The different supercell periodicity result in electronic band structures with different numbers of bands and different folding.

ATOMICALLY RESOLVED SPECTRAL FUNCTIONS OF SUPERLATTICES

Figure 10 shows spectral functions (SFs) of (a) bulk Si and (b) bulk Ge, and the progression of SFs of representative Si/Ge superlattices with decreasing period: (c) $\text{Si}_{26}\text{Ge}_{26}$, (d) $\text{Si}_{20}\text{Ge}_{20}$, (e) $\text{Si}_{12}\text{Ge}_{12}$, (f) Si_6Ge_6 , and (g) Si_4Ge_4 , respectively. Column (i)'s of rows (c)-(h) repre-

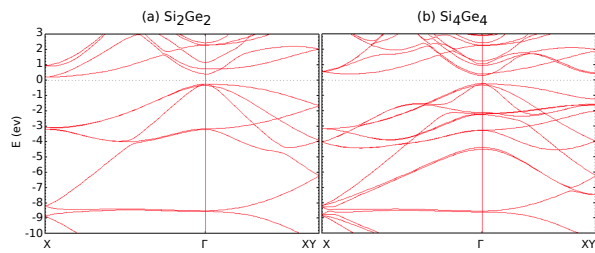


FIG. 9. Supercell band structure representative superlattices. (a) Si_2Ge_2 and (b) Si_4Ge_4 .

sent the total SFs and the columns (ii) and (iii) represent ASFs for atoms in the inner Si regions (red) and the inner Ge atoms (blue) of the superlattices, respectively. We show the inner Si and the Ge ASFs separately, to highlight how ASF differs for different atoms within the same superlattice.

TRAINING FORWARD AND REVERSE ML MODELS

The importance of features for the RF model is shown in Fig. 11. As shown in the figure, b_x is of the highest importance, as it is the measure of the strain in the plane that induces band splittings. b_z is the next most important feature that reflects different interatomic distances due to different atom types in the configuration. Interestingly, higher-order parameters are of higher importance; we attribute that to their sensitivity to the presence of material interfaces. The importance of atom type feature is low, which can be explained by the fact that only two atom types are considered. The other features can distinguish the atomic environments indirectly. However, this may change if many atomic species are present in the training configurations.

The learning curves during the training of the forward NN and reverse CNN models are shown in Fig. 12 and Fig. 13, respectively. MAEs change as we change the number of epochs of the model. We select the epoch with the lowest validation set MAE (red curves). In this article, we present the results obtained with epoch 4700 and 1750 for the forward NN and CNN models, respectively. However, the choice of these numbers is arbitrary.

FORWARD LEARNING MODEL PREDICTIONS FOR A TEST SUPERLATTICE

Figure 14 shows the performance of the forward learning model for a test superlattice, $\text{Si}_{28}\text{Ge}_{28}$, that is not included in the training set.

TEST OF REVERSE LEARNING MODEL

Heterostructure: We test the performance of the reverse learning model on the multilayer heterostructure, $\text{Si}_{28}\text{Ge}_{28}$. The chosen configuration is strain-symmetrized. We show the CNN-predicted descriptors for all atoms of the heterostructure in Fig. 15.

Bulk systems: We consider bulk Si and bulk Ge models grown on $\text{Si}_{1-x}\text{Ge}_x$ substrate with varied concentrations, x , which induces four different strains: 0.00%, 0.59%, 1.16%, 1.73%. We refer to strained Si and Ge as s-Si and s-Ge, respectively. It is important to note that the training set only includes superlattices and does not include any information on pristine bulk material. The bulk SFs are provided to the reverse learning model as input. We show the CNN-predicted descriptors in Table 5.

TABLE 5. Computed and Predicted Si Descriptors

| Test image | type | b_x | b_z | Q_x^1 | Q_z^1 | Q_x^2 | Q_z^2 | Q_x^3 | Q_z^3 |
|---------------------|------|-------|-------|---------|---------|---------|---------|---------|---------|
| Si | DFT | 1.00 | 2.58 | 2.58 | 1.00 | 1.00 | 1.00 | 1.00 | 1.00 |
| | CNN | 1.00 | 2.62 | 2.62 | 0.98 | 0.98 | 0.97 | 0.99 | 0.89 |
| | Err | 0.01 | 0.01 | 0.01 | 0.09 | 0.10 | 0.07 | 0.06 | 0.09 |
| s-Si [1] (0.59%) | DFT | 1.00 | 2.58 | 2.60 | 1.00 | 1.00 | 1.00 | 1.00 | 1.00 |
| | CNN | 1.00 | 2.61 | 2.63 | 0.92 | 0.92 | 0.90 | 0.92 | 0.82 |
| | Err | 0.01 | 0.01 | 0.01 | 0.18 | 0.19 | 0.15 | 0.15 | 0.18 |
| s-Si [2] (1.16%) | DFT | 1.00 | 2.57 | 2.61 | 1.00 | 1.00 | 1.00 | 1.00 | 1.00 |
| | CNN | 1.00 | 2.60 | 2.64 | 0.95 | 0.95 | 0.95 | 0.96 | 0.87 |
| | Err | 0.01 | 0.01 | 0.01 | 0.12 | 0.13 | 0.10 | 0.10 | 0.12 |
| s-Si [3] (1.73%) | DFT | 1.00 | 2.57 | 2.63 | 1.00 | 1.00 | 1.00 | 1.00 | 1.00 |
| | CNN | 1.00 | 2.60 | 2.66 | 0.97 | 0.96 | 0.96 | 0.97 | 0.90 |
| | Err | 0.01 | 0.01 | 0.01 | 0.11 | 0.12 | 0.11 | 0.11 | 0.13 |

The CNN model predicts atom type = 1 (type = 0) for all test structures of Si (Ge). The model is able to perceive the absence of Ge (or Si), even though all ASF training data include Ge (or Si) signatures. The identical b_x and b_z are also accurately predicted for relaxed bulk Si and Ge. The applied in-plane strains directly affect the bond lengths; b_z 's increase with higher in-plane tensile strains. The CNN model predicts atom type = 1 for all test structures of Si. The model is able to perceive the absence of Ge, even though all ASF training data include Ge signatures. The identical b_x and b_z are also accurately predicted for relaxed bulk Si. The applied in-plane strains directly affect the bond lengths; b_z 's increase with higher in-plane tensile strains. It is remarkable that the predicted order parameters are all close to the bulk values (~ 1), even in highly strained systems. This result indicates that order parameters are highly effective in distinguishing mixed environments from pristine ones.

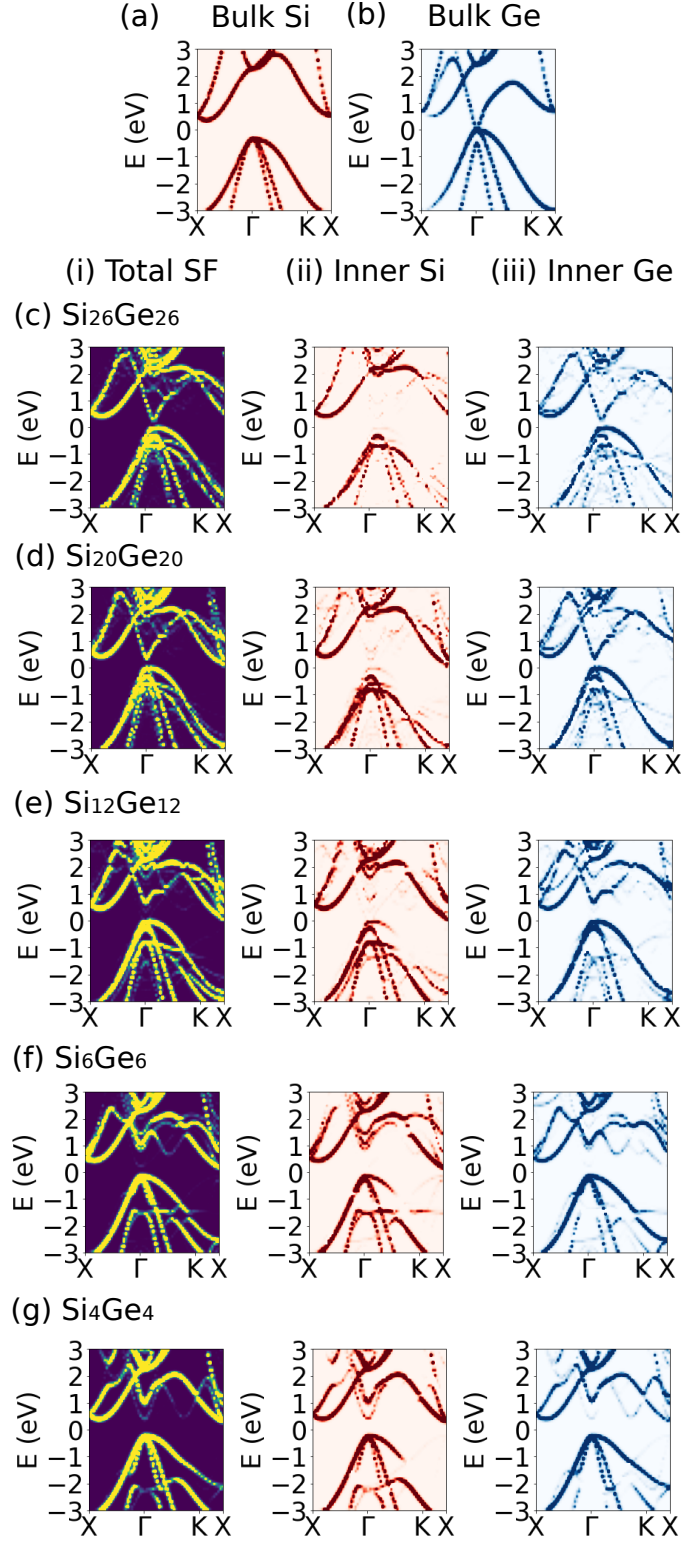


FIG. 10. Example spectral functions (SFs) of Si/Ge systems investigated in this work: SFs of bulk (a) Si and (b) Ge. (i) Total SFs and ASFs of (ii) inner Si and (iii) inner Ge atoms in (c) $\text{Si}_{26}\text{Ge}_{26}$, (d) $\text{Si}_{20}\text{Ge}_{20}$, (e) $\text{Si}_{12}\text{Ge}_{12}$, (f) Si_6Ge_6 and (g) Si_4Ge_4 superlattices.

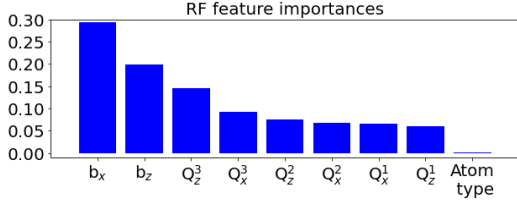


FIG. 11. Ranking of importance of different features in RF model.

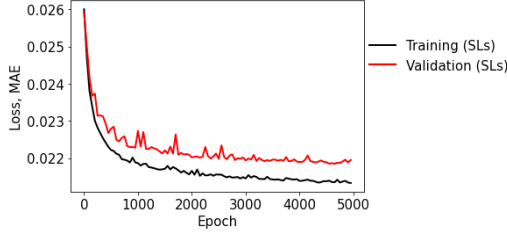


FIG. 12. Learning curves for NN.

MACHINE LEARNING MODEL DETAILS

The details of the ML models are shown in Table 6 and Table 7 below.

EFFECTS OF FERMI-LEVEL ALIGNMENT

It is known that the PBE-GGA approach fails to accurately predict the band gaps of semiconductors. We show a comparison between the PBE-GGA band structures and those obtained with GW calculations [62] (black dashed line) in Fig. 17. The valence bands obtained with the PBE-GGA approach match the GW results; however, the conduction bands are lowered, resulting in an underestimated band gap. Such discrepancies have been extensively discussed [19, 20, 63–65]. However, the PBE-GGA approach has been widely used to predict the electron/hole transport properties of semiconductors, including the biaxial strain enhanced in-plane mobility in

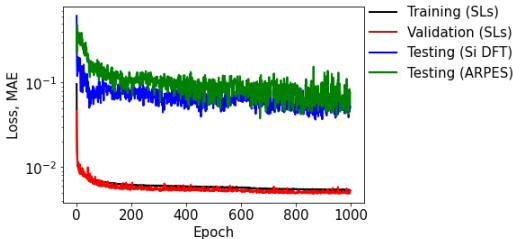


FIG. 13. Learning curves for CNN.

TABLE 6. NN model for forward learning

| Layer | Nodes | Parameters |
|-------|--------------------------|------------------------------|
| Dense | (16) | input dimension = 9 features |
| | | $f_a = \text{ReLU}$ |
| Dense | (32) | $f_a = \text{ReLU}$ |
| Dense | (6144) | $f_a = \text{Linear}$ |
| | $64 \times 96 A^p(k, E)$ | |

TABLE 7. Reverse CNN block

| Layer | Shape | Parameters |
|---------------------|---------------------|-----------------------|
| CoordinateChannel2D | (64, 64, 4) | — |
| Conv2D | (32, 32, 8) | $k=3, s=2$ |
| | | $f_a = \text{ReLU}$ |
| BatchNormalization | — | — |
| Conv2D | (16, 16, 8) | $k=3, s=2$ |
| | | $f_a = \text{ReLU}$ |
| BatchNormalization | — | — |
| Conv2D | (8, 8, 8) | $k=3, s=2$ |
| | | $f_a = \text{ReLU}$ |
| BatchNormalization | — | — |
| Flatten | (512) | — |
| Dense | (16) | $f_a = \text{ReLU}$ |
| Dense | (8) | $f_a = \text{ReLU}$ |
| Dense | ($n = 9$ features) | $f_a = \text{Linear}$ |

k: kernel size, s: stride size, f_a : activation function

Si [38] and the thermoelectric properties of Si [18, 39] and Si/Ge superlattices [19–23, 40]. In previous publications, we compared the electronic transport properties [20] predicted using PBE functionals and Heyd-Scuseria-Ernzerhof [66]. Through a systematic analysis, we illustrated the effectiveness of the PBE-GGA approach to predict the relationship between the lattice environment and the electronic properties of semiconductor heterostructures. In this article, our objective is to develop a model for the rapid prediction of this relationship. The computational cost of alternative approaches such as using hybrid functionals [67, 68] or implementing GW calculations [62] prohibits the use of these approaches to analyze large structures, especially for data-driven studies. Furthermore, previous studies provide the necessary justification for using the PBE-GGA approach to establish the model.

Here, we use data obtained with the PBE-GGA approach to train ML models. We discuss the role of Fermi-level alignments on ML predictions. To obtain the results shown in main manuscript, we use one Fermi level alignment for the forward learning level, but different Fermi level alignments for the reverse learning model.

Forward Learning Approach: We assign the Fermi-level ($E = 0$ level) to be equal to the middle of the band gap value, to obtain the total SF for each training configuration. The ASFs are shifted by the corresponding amount and the forward learning model is trained with the resulting ASFs. We show the predicted ASFs and the total SFs of the test superlattices and heterostructures in Fig. 14

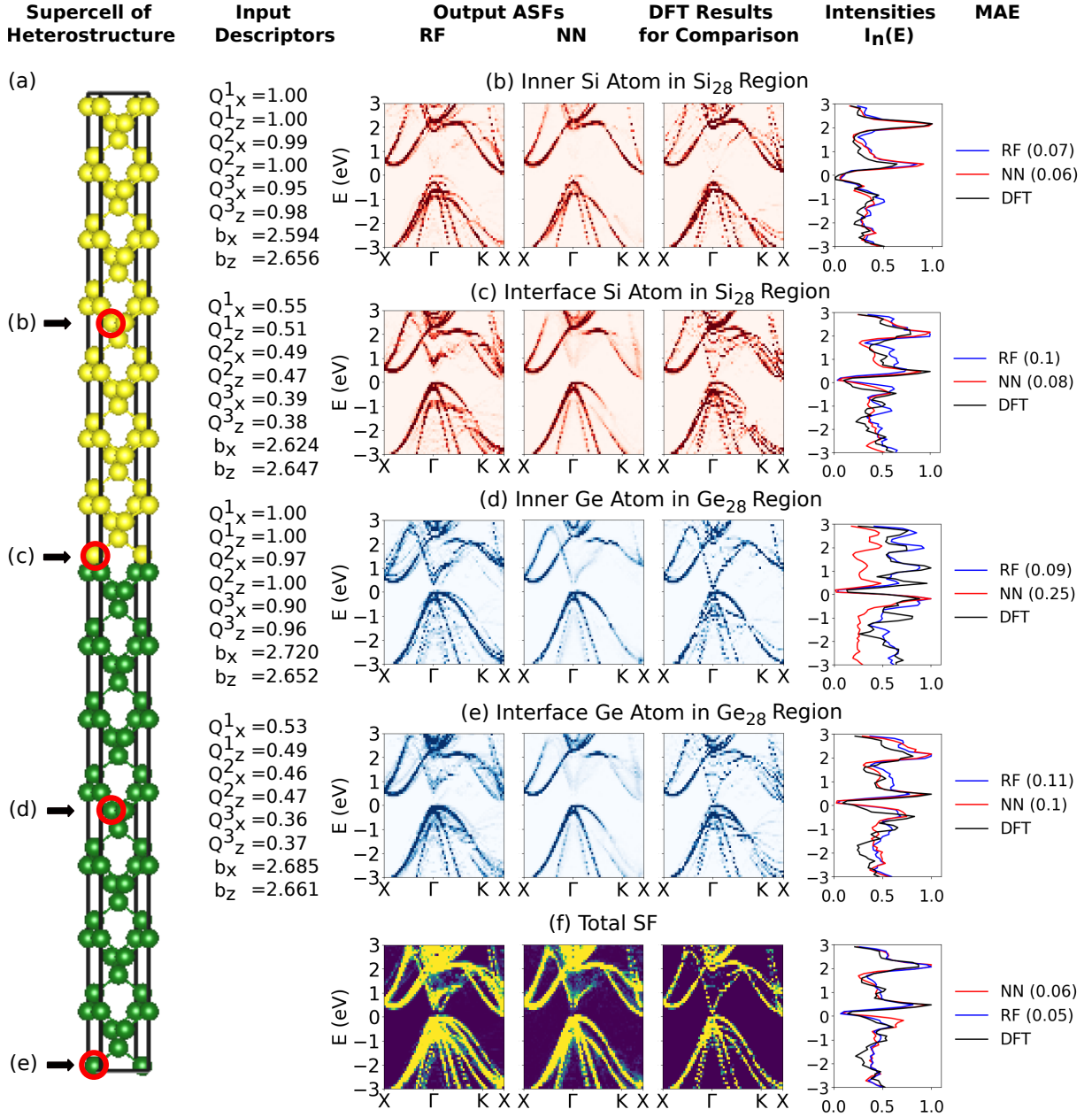


FIG. 14. **Forward learning model predictions:** (Column 1) (a) Representative supercell configuration of test superlattice, $\text{Si}_{28}\text{Ge}_{28}$, and selected atoms from (b) inner Si_{28} , (c) $\text{Si}_{28}\text{Ge}_{28}$ interface, (d) inner Ge_{28} , and (e) $\text{Ge}_{28}\text{Si}_{28}$ interface; (Column 2) Atomic descriptors of chosen atoms provided as input to forward model; (Column 3 & 4) Output ASFs of chosen atoms predicted by RF and NN models, respectively. (Column 5) ASFs of representative atoms computed directly with DFT for comparison and validation. (Column 6) Comparison between normalized intensities, $I_n(E)$, and (Column 7) MAEs for NN (red) and RF (blue) predictions. (f) Total SFs obtained by summing over ASFs of all atoms of superlattice.

and Fig. 3 of main manuscript, respectively. As can be seen from the figures, both predicted energy bands and energy level alignments are in good agreement with the corresponding DFT results.

Different Fermi-level Alignments: We illustrate the change of ML predictions by varying alignments of training ASFs.

(Case I) Electronic band gap cannot be directly defined for the ASFs, to the best of our knowledge. We align the Fermi-level of each ASF of training superlattice to the respective mid-band-gap level. We task the trained ML model to predict ASF (or total SF in this case) for bulk Si systems. Bulk systems include atomic environments which is not present in the training structure. Re-

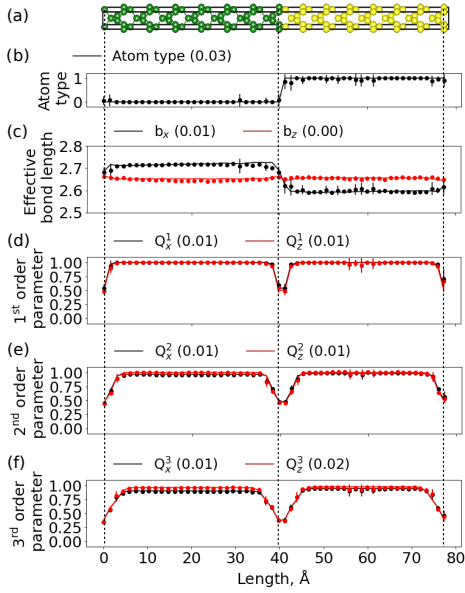


FIG. 15. **Reverse learning model predictions for strain-symmetrized $\text{Si}_{28}\text{Ge}_{28}$ superlattice:** (a) Supercell configuration; Predicted (b) atom type, (c) effective bond length and (d-f) spatially resolved order parameters, Q_i^{order} where $i = (x, z)$ and $order = 1, 2, 3$. MAEs between predicted (circles) and calculated features (solid lines) are shown within parentheses in legends.

call that our training set only includes structures with a mixture of both materials. As we illustrate below, the Fermi-level alignment of the ASF training data strongly affects the predictions in this case. Figure 18 shows the SFs of (a) relaxed and (b) strained Si. The first and the second column show the SFs predicted by the NN and the RF models, respectively. The third column represents DFT results. We show the comparison between predicted and computed $I_n(E)$'s in the last column and report the MAEs. The mismatch between Fermi-levels is pronounced in the plot showing the normalized intensities for strain-symmetrized bulk Si. Interestingly, the predictions are in good agreement with the DFT SF results for bulk Si with in-plane strain.

(Case II) We align ASFs such that the zero-energy level of each ASF corresponds to the largest spectral weight at the Γ -point in the valence zone or valence band maximum (VBM). We retrain the model with VBM aligned-ASFs and task the model to predict ASFs for the bulk systems. The predictions are shown for relaxed and strained bulk Si systems in Fig. 18(c,d). In this case, both the peak intensities and the energy alignments are reproduced with a good agreement with DFT results.

(Case III) We align the total SF of each training superlattices such that the zero-energy level is set to the largest spectral weight at the Γ -point in the valence zone or VBM. The energy bands of ASFs are shifted by the

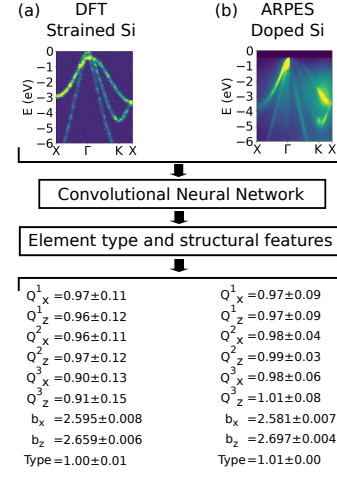


FIG. 16. **Reverse learning model predictions.** Input images: (a-b) DFT predicted ASFs for (a) substrate-strained (s-Si) bulk Si and (b) ARPES spectra of doped Si thin film, adopted from Ref. 44. CNN extracts atomic environment descriptors from input. Standard deviations are calculated for various Fermi level alignments and gamma-corrections (power transformations).

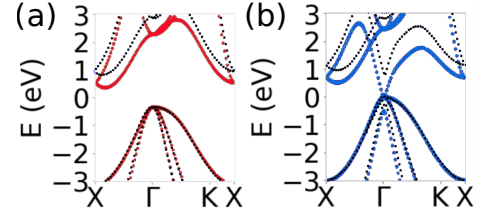


FIG. 17. **Band structures** of (a) bulk Si and bulk Ge obtained with PBE-GGA approach (solid lines). The dotted black lines represent results from GW calculation from literature [62].

corresponding amount. The ML predictions for the bulk systems are shown in Fig. 18(e,f). The NN predicted relaxed Si bands are better aligned than RF, however the spectral weights are diminished for the NN predictions. The predictions for both relaxed and strained Si are worse than the ones reported for case (II).

As can be observed from above discussion, the ML predictions vary in an unpredictable manner depending on the energy level alignments of training ASFs. To generalize and diversify the training set for the reverse learning model, we consider 13 Fermi level alignments in incremental steps in the range from +0.5 eV to -0.5 eV from the mid-gap energy level. The various alignments correspond to different electron doping in ARPES experiments.

Reverse Learning Model: We test the CNN model to predict the descriptors of bulk Si systems when the SF images are provided as input. We use two categories

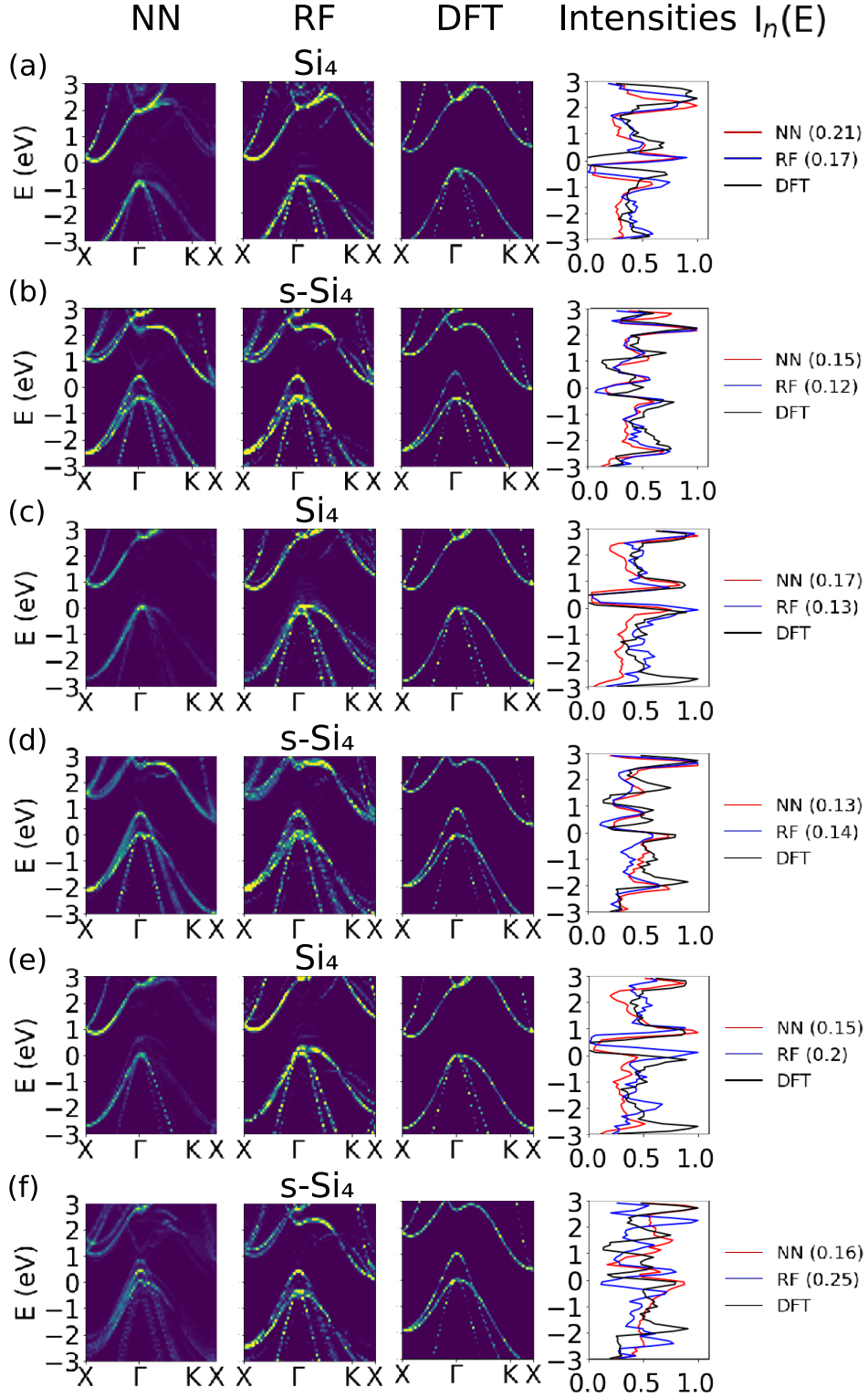


FIG. 18. **Effect of Fermi-level alignment of training ASF data on ML performance:** (a-b) ASFs with Fermi-level aligned at the mid gap level. Predicted SFs for (a) relaxed bulk Si and (b) bulk Si in tensile strain due to Ge substrate. ASFs with Fermi-level aligned at VBM, independently for each ASF: Predicted SFs for (c) relaxed and (d) strained bulk Si. ASFs with Fermi-level aligned at VBM, independently for each total SF: Predicted SFs for (e) relaxed and (f) strained bulk Si.

of test images: the DFT predicted SFs of relaxed and strained bulk Si and a spectra obtained from ARPES experiment. In practice, only the valence bands may be available in the ARPES experimental images. To adapt to such constrains, we train the reverse ML model with the energy levels of DFT results below the VBM level. In other words, the ASFs are aligned individually such that the zero-energy level corresponds to the largest spectral weight at the Γ -point in the valence zone. As discussed

above, the band gap is not directly defined for the ASF, so the shift in the Fermi level is ambiguous. This provides a way to expand the training data set by applying various amount of shifts. The CNN model is then trained on the corresponding ASFs. The CNN approach has shown high level of efficiency with image data sets. We expect the CNN model to capture unique patterns in the ASF rather than the shift associated with the different Fermi-level alignments.